Assessing the capability of Sentinel-2 time-series to estimate soil organic carbon and clay content at local scale in croplands

Fabio Castaldi, Muhammed Halil Koparan, Johanna Wetterlind, Renaldas
Žydelis, Ialina Vinci, Ayşe Özge Savaş, Cantekin Kıvrak, Tülay Tunçay, Jonas
Volungevičius, Silvia Obber, et al.

HAL Id: hal-04065076
https://hal.inrae.fr/hal-04065076

Submitted on 11 Apr 2023

Contents lists available at ScienceDirect

ISPRS Journal of Photogrammetry and Remote Sensing

journal homepage: www.elsevier.com/locate/isprsjprs
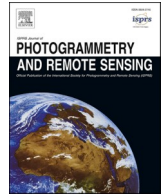
Assessing the capability of Sentinel-2 time-series to estimate soil organic carbon and clay content at local scale in croplands

Fabio Castaldi [a,*], Muhammed Halil Koparan [b], Johanna Wetterlind [c], Renaldas Žydelis [d], Ialina Vinci [e], Ayşe Özge Savaş [b], Cantekin Kıvrak [f], Tülay Tunçay [b], Jonas Volungevičius [d], Silvia Obber [e], Francesca Ragazzi [e], Douglas Malo [g], Emmanuelle Vaudour [h]

[a] *Institute of BioEconomy, National Research Council of Italy (CNR), Via Giovanni Caproni 8, 50145 Firenze, Italy*
[b] *Soil, Fertilizer and Water Resources Central Research Institute Ankara, Turkey*
[c] *Swedish University of Agricultural Sciences, Department of Soil and Environment, Skara, Sweden*
[d] *Institute of Agriculture, Lithuanian Research Centre for Agriculture and Forestry, Lithuania*
[e] *Environmental Protection Agency of the Veneto Region (ARPAV), Italy*
[f] *Atatürk Soil Water and Agricultural Meteorology Research Institute, Kırklareli, Turkey*
[g] *South Dakota State University, Department of Agronomy, Horticulture & Plant Science, Brookings, SD, USA*
[h] *Université Paris-Saclay, INRAE, AgroParisTech, UMR EcoSys, 91120 Palaiseau, France*

ARTICLE INFO

ABSTRACT

The use of remote sensing data methods is affordable for the mapping of soil properties of the plowed layer over croplands. Carried out in the framework of the ongoing STEROPES project of the European Joint H2020 Program SOIL, this work is focused on the feasibility of Sentinel-2 based approaches for the high resolution mapping of topsoil clay and organic carbon (SOC) contents at the within-farm or within-field scales, for cropland sites of contrasted climates and soil types across the Northern hemisphere. Four pixelwise temporal mosaicking methods, using a two years-Sentinel-2 time series and several spectral indices (NDVI, NBR2, BSI, S2WI), were developed and compared for *i)* pure bare soil condition (maxBSI), *ii)* driest soil condition (minS2WI), *iii)* average bare soil condition (Median) and *iv)* dry soil conditions excluding extreme reflectance values (R90). Three spectral modeling approaches, using the Sentinel-2 bands of the output temporal mosaics as covariates, were tested and compared: (*i*) Quantile Regression Forest (QRF) algorithm; (*ii*) QRF adding longitude and latitude as covariates (QRFxy); (*iii*) a hybrid approach, Linear Mixed Effect Model (LMEM), that includes spatial autocorrelation of the soil properties. We tested pairs of mosaic and spectral approaches on ten sites in Türkiye, Italy, Lithuania, and USA where soil samples were collected and SOC and clay content were measured in the lab. The average RPIQ of the best performances among the test sites was 2.50 both for SOC (RMSE = 0.15%) and clay (RMSE = 3.3%). Both accuracy level and uncertainty were mainly influenced by site characteristics of cloud frequency, soil types and management. Generally, the models including a spatial component (QRFxy and LMEM) were the best per-forming, while the best spatial mosaicking approaches mostly were Median and R90. The most frequent optimal combination of mosaicking and model type was Median or R90 and QRFxy for SOC, and R90 and LMEM for clay estimation.

1. Introduction

For more effective farm management, updated soil maps of soil properties are crucial, and there is increasing demand for up-to-date and detailed soil information for the adoption of agricultural practices that are recommended through several policies (Tziolas et al., 2021), especially in the framework of European Green Deal, Common Agricultural Policy (CAP), EU Soil Thematic Strategy, and Food Safety and Food Security (FAO) programs (Chabrillat et al., 2019). For instance, the so-called "carbon farming" approaches need accounting for soil carbon estimation and changes to efficiently manage soil carbon storage (Brockett et al., 2019). However, the implementation of these ap-proaches raises some issues related to the mapping of the soil properties and its updating over time in conjunction with agronomic and climatic

dynamics which influence the evolution of soil properties such as soil organic carbon (SOC) content. In this regard, satellite approaches in the optical domain are not only promising but also affordable, for deriving a number of soil properties of the ploughed layer over croplands, especially SOC at several scales from local to national and higher (Vaudour et al., 2022). Indeed, along with clay, iron, calcium carbonate and soil moisture, SOC content is one of the most influential properties on the reflectance of bare soil surface in the visible-near infrared-shortwave infrared domains (400–2500 nm) (Ben-Dor, 2002; Chabrillat et al., 2019) and hence one of the most easily quantifiable via remote sensing. According to a recent cost-accuracy analysis (Andries et al., 2021), a combination of earth observation technology and in situ sampling has the potential to offer a reliable, cost-effective approach for monitoring and reporting of SOC stocks at local scale, i.e within-farm or within-field-scale.

While SOC strongly influences soil surface reflectance, it shall be mentioned that such relation is very straightforward for dry samples of 2 mm-sieved fine earth in the lab, but far more complex for undisturbed topsoil in the field, especially for cultivated soils with soil technical operations modifying its mineral and organic composition as well as the microtopography of the soil surface and the vegetation lying on it, having direct impact for satellite approaches (Vaudour et al., 2022). The feasibility of satellite-based digital mapping of topsoil properties raises several interconnected issues related not only to soil surface condition, the influence of soil composition according to soil type, the influence of soil management practices, but also to sampling design (Castaldi et al., 2019b), and finally the availability of adequate reflectance image spectra over time. Spectral models relating image reflectance spectra of bare soils with topsoil properties may rely on a single-date image (e.g. Gholizadeh et al., 2018; Mzid et al., 2022) or on a composite image made of several dates, a temporal mosaic of a satellite time series (Castaldi, 2021; Dvorakova et al., 2021; Vaudour et al., 2021; Shi et al., 2022). In this regard, the frequency of cloudless satellite images affects the possibility of acquiring pixels with bare soils across a time-series over the entire fields and/or farm. Indeed, according to both soil surface and weather conditions, single-date images are prone to varying SOC prediction performance (Vaudour et al., 2019; Urbina-Salazar et al., 2021; Dvorakova et al., 2021) and the use of a time-series is more likely to identify the optimal dates for SOC mapping. Furthermore, for annual cropping systems, the extent of bare soil exhibits seasonal changes according to crop rotations.

Bare soils are usually delineated by thresholding a spectral vegetation index, the Normalized Difference Vegetation Index (NDVI) being the index commonly employed for such a purpose (Vaudour et al., 2022). Other spectral indices may be used to identify the bare soils pixels with the least possible influence of other disturbing factors besides green vegetation, such as Normalized Burn Ratio 2 (NBR2) which aims to discard those pixels having dry vegetation on the surface (Castaldi et al., 2019a), or soil moisture index (S2WI) that aims to discriminate between very moist bare soils and other bare soils (Vaudour et al., 2019), or the bare soil index (BSI) that has been mainly conceived to discriminate between bare soil and other land covers (Diek et al., 2017; Rikimaru et al., 2002). With the aim to detect bare soil with minimum topsoil roughness, Dvorakova et al. (2021) successfully tested the greening-up approach over Sentinel-2 collection to select images acquired at seedbed conditions using both NDVI and NBR2 indices. Vaudour et al. (2021) obtained improved SOC prediction accuracy when combining the use of NDVI, NBR2 and S2WI indices, nevertheless the threshold value for these indices required to drop a large part of the cropland pixels.

As the extent of bare soil varies seasonally, particularly under annual cropping systems, soil rarely appear as bare over an entire farm area at a given single date. Temporal mosaics enable extending the bare soil area and consequently increasing the soil properties mapping area by mosaicking the available images. In this regard, the short revisit time of the NASA and Copernicus-ESA multispectral satellite missions, Landsat

8 and Sentinel-2, respectively, make it possible for large satellite collection in a short period of time. This increases the chance of finding cloud-free images at bare soil condition (Castaldi, 2021; Demattê et al., 2018). Temporal mosaicking may rely on per-pixel reflectance averaging (e.g. Demattê et al., 2018) or index minimizing or maximizing (e. g. Loiseau et al., 2019; Vaudour et al., 2021) across a time series. As disturbing factors such as soil moisture or vegetation cover may vary with time, the incorporation of pixels from dates with "bad conditions" into a given mosaic may jeopardize reflectance-based models of soil properties (Vaudour et al., 2021). Amongst those topsoil conditions which can be considered "bad", or unfavorable for a reasonably accurate soil property prediction, soil moisture is considered key (Stenberg et al., 2010): it leads to worsen SOC prediction models, as verified in lab conditions (Rienzi et al., 2014; Cao et al., 2020; Mirzaei et al., 2022; Knadel et al., 2022). As soil surface conditions vary at several time steps, especially hourly, the retrieval of soil moisture is tricky. There exist soil moisture products derived from Sentinel-1 and semi-empirical radar model inversion (El Hajj et al., 2017), which proved to facilitate the identification of driest dates for efficient temporal mosaicking at regional scale (Vaudour et al., 2021); however, Sentinel-1 images are not acquired at the very date and hour of the Sentinel-2 images, and such soil moisture products are not currently available across the world. In this study, it is assumed that spectral indices related to soil moisture absorption bands such as S2WI or NBR2 might be used as easily available proxies of soil moisture derived from Sentinel-2. Furthermore, because the drier the soil the higher is soil reflectance, we tested a completely new approach assuming that the spectra reaching the 90-percentile reflectance values across a given time series are those exhibiting the driest soil surface condition while excluding extreme values which may be due to clouds or snow cover.

Validating model performance and the resulting maps is important in all modeling approaches in order to evaluate the usefulness for practical applications or for comparisons between models (Piikki et al., 2021), as well as to comply with the Global Soil Map requirements (Arrouays et al., 2014). Accuracy, defined as a measure of how close the predictions are to known values, but also model stability, or uncertainty, often defined in spatial models as the expected, or observed, variation in the predictions, are important and can give valuable information about generalization and applicability of the models. Through the geostatistical approach, the production of the quantitative accuracy map is inherent in the model and usually expressed as the variance of the expected value. Uncertainty of soil properties prediction and soil mapping is generally underestimated or most often not shown (Arrouays et al., 2014; Vaysse and Lagacherie, 2017). Other approaches such as Quantile Regression Forests (QRF), considering the spread of the response variable from which prediction intervals are constructed, are recommended as they provide accurate and interpretable predicted patterns of uncertainty (Vaysse and Lagacherie, 2017).

Carried out in the framework of the ongoing STEROPES project of the European Joint H2020 Program SOIL (https://ejpsoil.eu/soil-research/steropes/https://ejpsoil.eu/soil-research/steropes/), this paper is focused on the feasibility of Sentinel-2 based approaches for the detailed mapping of topsoil clay and SOC contents at the local field scale, compatible with carbon farming approaches. Most satellite approaches of SOC mapping have been carried out in Temperate agroecosystems, at the scale of small regions covering some tens of km^2 and a limited range of soil types dominated by Luvisols and Cambisols (Vaudour et al., 2022). To the best of our knowledge, the previous local scale studies that have been carried out, have not included in the same study several environmental conditions (climate and soil type) and cropping systems. This study tests the robustness of such spectral approaches across a dataset encompassing varied annual cropping systems covering semi-arid, temperate to temperate continental and close to boreal climates and a large variation in soil types including the above-mentioned dominant soil types as well as other less often studied soil types: Fluvisols, Vertisols, Chernozems, Gleysols, Retisols. Calcisols. Previous

studies highlighted the need to fine-tune the methods for mosaicking bare soil pixels from large satellite collections (Castaldi, 2021; Dvorakova et al., 2021), thus finding a deal between accuracy/uncertainty and spatial coverage of soil propertie maps. In accordance with the above-mentioned research lines, our approach is original in developing and comparing four pixelwise temporal mosaicking methods aiming for *i)* pure bare soil condition, *ii)* driest soil condition, *iii)* average bare soil condition and *iv)* driest soil conditions excluding extreme reflectance values. Knowing that the predicted soil properties from Sentinel-2 exhibit spatial structure (Castaldi et al., 2019c), three modeling approaches were tested, two Quantile Regression Forest (QRF) algorithms were used with one including longitude and latitude coordinates, and a third hybrid model, the Linear Mixed Effect Model (LMEM), that includes spatial autocorrelation of the soil properties was tested and compared. Both types of models provide measurements of the uncertainty of the model predictions which were further used in the analysis to evaluate the capabilities of the different combinations of mosaicking methods and prediction models.

Hence our approach is trifold: i) testing local approaches in ten fields within four agroecosystems with annual crops; ii) elaborating a new temporal mosaicking for use in such local context; iii) accounting for spatial uncertainty as recommended for digital soil mapping.

2. Materials and methods

2.1. Study areas and soil dataset

The sites that were collected for this study were sites available through a trade-off between agroecosystem diversity, spatial density and also the recent collection period for the SOC analyses, known to be influential for SOC prediction accuracy (Urbina-Salazar et al., 2021). For all sites (Fig. 1), climate is described according to the Köppen climate classification (Peel et al., 2007). Soil types are named according to the Word Reference Base (IUSS Working Group WRB, 2015). Site location (longitude and latitude), climate region and main soil types, for each test site, are summarized in Table 1. Türkiye and USA sites cover areas and sampling densities ranging from 102 to 425 ha and from 0.3 to 0.8 samples/ha respectively; Italian sites cover about 30 ha each with a sampling density close to 2 samples/ha while Lithuanian sites extent is around 2 ha only with the highest sampling density close to 25 samples/ha (Fig. 2).

2.1.1. Turkish test sites

Two agricultural areas, Dalaman (TUR_DAL) and Kocas (TUR_KOC), were chosen in Türkiye regarding their different climatic conditions, soil characteristics, SOC content, soil and crop management (Fig. 1; Table 1).

TUR_DAL site is located in the south-western part of Türkiye near the Aegean Sea in alluvial deposits. The climate of the region is classified as Hot-summer Mediterranean climate (Csa) with an annual precipitation of 1030 mm and mean temperature of 18.1 °C (mean values over the 30 years period). Common soil type in the study area is Calcaric Fluvisols (Drainic). In the sampling area both corn (*Zea mays L.)* -wheat (*Triticum aestivum L.*) or wheat- sunflower (*Helianthus annuus L.*) crops are raised in the same year.

TUR_KOC study area is located in the alluvial deposits of the Konya Closed Basin, 30 km southeast of Salt Lake (Tuz Gölü). The climate is classified as a Cold semi-arid climate (Bsk) with an average annual precipitation of 362 mm and temperature of 12.2 °C (mean values over the 30 years period). The common soil types in this area are Calcaric Fluvisols (Drainic) and Eutric Vertisols. The main crops are irrigated corn and wheat with annual rotation.

Soil sampling was done in summer 2021 (Fig. 2) in both study areas regarding soil types and sampling locations in order to achieve an evenly distribution through the field. Each sample consisted of three sub-samples taken with a gouge auger within an area of a 3 m radius and collected from 0 to 20 cm depth. Soil samples were air dried and passed through a 2 mm sieve in the laboratory, and SOC was determined following the Walkley-Black oxidation method. The particle size distribution analysis was done using the hydrometer method (Bouyoucos, 1951). Soil conditions at the sampling time were bare with some plant residue leftover from previous year. The Turkish samples are characterized by low SOC content of 1.08 and 0.8 % in average for TUR-KOC and TUR_DAL, respectively, and dominant clayey texture but considerable within-field variations, particularly for TUR-KOC (clay content ranging from 15 to 67%) (Table 2). Clay and sand are highly correlated in both sites, while the correlation between SOC and clay, and SOC and sand is significant only in TUR_DAL (Table 3).

2.1.2. USA test sites

Five fields in croplands were selected in the USA: three fields located in Brookings County, South Dakota (USA_SDA), and two fields located in Lac qui Parle County, Minnesota (USA_MIN). The climate in South Dakota is classified as Monsoon Influenced hot summer humid continental climate, with an average annual precipitation of 686 mm, hot summer and dry winter (Dwa). For Minnesota it is a warm summer humid continental climate (Dfb) with an average annual precipitation of 660 mm and no dry season. Mean annual air temperature is 6,4 and 6.9 °C for USA_SDA and USA_MIN, respectively. USA_SDA fields are located on the loamy till and loamy eolian deposits, while USA_MIN fields are on lacustrine and loamy glaciofluvial deposits. For both sites, the dominant soils are Haplic Chernozem (Pantoarenic, Aric), Calcic Chernozem (Pantoloamic, Aric, Cambic), and Chernic Gleysol
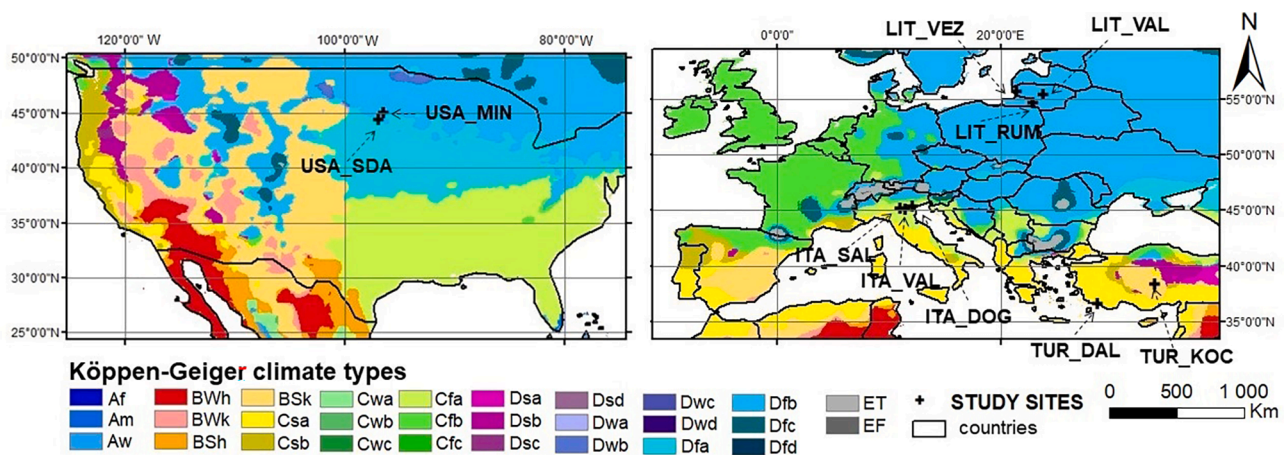

Fig. 1. Map of Köppen-Geiger climate types (adapted from Peel et al., 2007) and location of the test sites where the soil datasets were collected.

Table 1

Site location, climate region according Köppen climate classification and main soil types for each test site.

| Country	Site	Longitude (decimal degrees)	Latitude (decimal degrees)	Koppen climate classification	Main soil types
Türkiye	TUR_KOC	33.87138 E	38.41498 N	Bsk	Calcaric Fluvisols; Eutric Vertisols
	TUR_DAL	28.78039 E	36.71582 N	Csa	Calcaric Fluvisols
USA	USA_SDA	−96.8709 E	44.3864 N	Dwa	Haplic Chernozem; Calcic Chernozem; Chernic Gleysol
	USA_MIN	−96.44499 E	45.07500 N	Dfb	Haplic Chernozem; Calcic Chernozem; Chernic Gleysol
Italy	ITA_SAL	11.074774 E	45.244738 N	Cfa	Haplic Luvisols; Hypereutric Cambisol
	ITA_VAL	11.495782 E	45.161852 N	Cfa	Calcaric Gleysols; Haplic Calcisols
	ITA_DOG	12.163741 E	45.400746 N	Cfa	Cambic Calcisols; Calcaric Calcic Gleysols
Lithuania	LIT_VEZ	21.460352 E	55.726941 N	Dfb	Glossic Albic Eutric Retisol; Epigleyic Albic Haplic Luvisol
	LIT_VAL	23.861952 E	55.380085 N	Dfb	Endogleyic Endostagnic Endocalcaric Luvisol
	LIT_RUM	22.997302 E	54.696184 N	Dfb	Endocalcaric Gleysol; Epigleyic Endocalcaric Cambisol
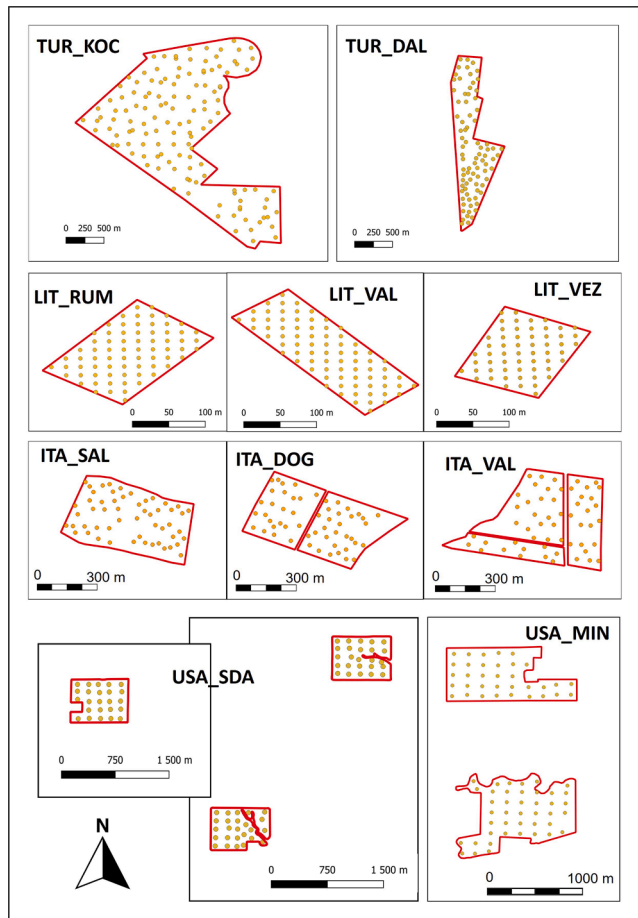
Fig. 2. Location of the soil samples collected within each test site for the determination of soil organic carbon and clay content.

(Pantoloamic, Aric, Colluvic, Drainic, Pachic). The main crops in both states are corn, soybean (*Glycine* max *L.*), sunflower, wheat and barley (*Hordeum vulgare L.*). At the study sites, a corn-soybean rotation has been followed for years. These fields cover the most common soil classes for both states. A 156 × 156 m soil sampling grid was used for each field with each collected soil sample representing 2.43 ha. Around five soil sub-samples were collected within a 3 m' radius of each grid-cell center and mixed for a composite sample at 15 cm depth, using a push probe in May 2018 (Fig. 2).

The SOC was determined using the loss on ignition method following the South Dakota State University (SDSU) Soil Testing and Plant Analysis Laboratory protocol (SDSU, 2006). This protocol estimates SOC based on gravimetric weight change associated with high-temperature oxidation of OC (Pribyl, 2010). The sampled soil was analyzed for particle-size distribution by hydrometer method according to SDSU Soil Testing and Plant Analysis Laboratory protocol (SDSU, 2006).

The two USA soil datasets are characterized by very similar and high SOC content (mean SOC: 2.54 %) and loam and clay loam soil texture (Table 2). The correlations between SOC, clay and sand contents are all significant for both USA datasets (Table 3).

Table 3

Pearson's correlation coefficient between soil properties. *Significant correlation ($P < 0.05$).

Site	SOC vs Clay	SOC vs Sand	Clay vs Sand
TUR_KOC	−0.06	0.13	−0.92*
TUR_DAL	**0.82***	**−0.65***	**−0.83***
USA_SDA	**0.92***	**−0.94***	**−0.95***
USA_MIN	**0.67***	**−0.76***	**−0.85***
ITA_SAL	0.08	−0.13	−0.86*
ITA_DOG	**0.66***	**−0.50***	**−0.83***
ITA_VAL	**0.52***	**−0.40***	**−0.91***
LIT_RUM	**0.65***	**−0.64***	**−0.31***
LIT_VAL	−0.16	**−0.39***	0.08
LIT_VEZ	**−0.32***	**−0.43***	−0.41*

Table 2

Basic statistics for SOC, clay and sand contents. Nb, number of soil samples.

	N° samples	Area (ha)	SOC (%)				Clay (%)				Sand (%)			
			Min	Max	Mean	Std	Min	Max	Mean	Std	Min	Max	Mean	Std
TUR_KOC	131	425	0.65	1.97	1.08	0.22	14.7	66.8	40.68	11.49	15.1	69.6	39.04	10.38
TUR_DAL	82	102	0.52	1.25	0.80	0.18	19.67	55.98	32.23	8.23	16.45	51.31	33.58	7.71
USA_SDA	74	177	1.05	3.63	2.54	0.69	8.1	41.85	25.24	9.89	9.97	75.59	44.44	20.31
USA_MIN	76	184	1.39	4.38	2.54	0.51	19.15	48.61	30.79	5.9	24.37	68.04	45.2	9.24
ITA_SAL	54	26	0.51	0.81	0.66	0.07	9.9	17	13.38	1.75	48.3	67	57.74	5.48
ITA_DOG	54	27.5	0.99	2.1	1.51	0.24	17.2	48.8	37.76	7.07	7	35.8	15.07	6.21
ITA_VAL	53	30.3	1	1.99	1.46	0.2	24.8	51.3	40.48	6.21	6	31.1	15.15	5.91
LIT_RUM	70	2.8	1	2.78	1.77	0.43	16.6	39.9	29.38	5.55	26.8	62.4	43.8	8.03
LIT_VAL	53	2.2	1.23	2.53	1.58	0.28	7.8	19.4	13.49	2.18	46.1	57.7	51.03	2.82
LIT_VEZ	57	2.3	1.3	2.22	1.78	0.23	6.01	16.2	10.64	2.17	41.4	66.7	48.24	4.55

2.1.3. Italian test sites

Three experimental fields in croplands were selected in the alluvial plain of the Veneto Region (Italy). All the three sites are in the Po Plain that has a Humid subtropical climate (Cfa): ITA_SAL, ITA_VAL, ITA_DOG. The average annual precipitations for the three sites range between 734 and 887 mm and mean temperature between 13.4 and 14 °C (mean values over the period 1994–2021). All soils derive from alluvial deposits. The main crops are corn, soybean, wheat and barley. For all the plots a 1:50.000 scale soil map was available (https://gaia.arpa.veneto.it/maps/778/view). Furthermore, a detailed soil survey in the plots was carried out at 1:10.000 scale.

The ITA_SAL plot is located in the middle reach of the Adige megafan formed during the Last Glacial Maximum (Fontana et al., 2014; Garlato et al., 2005), characterized by prevalent sandy deposits. Even though the parental materials were calcareous, soils are completely decarbonated; within the ITA_SAL plot, Haplic Luvisols (Aric, Cutanic, Differentic, Hypereutric, Loamic) have developed on well-drained surfaces, while on surfaces where the shallower aquifer has partially hindered pedogenesis Hypereutric Cambisols (Aric, Loamic, Oxyaquic) are to be found, with somewhat slower drainage.

The ITA_VAL plot is located in a more recent part of the alluvial plain of the Adige river (Early-Mid Holocene), in a depression between two river levees; within ITA_VAL plot, the soils developed in the finer material are Calcaric Gleysols (Aric, Pantoloamic, Humic) and those on fine-silty materials are Haplic Calcisols (Aric, Gleyic, Hypocalcic, Pantosiltic), both partially decarbonated and somewhat poorly drained.

Soils in the ITA_DOG plot are in the lower reaches of the Brenta megafan formed during the Last Glacial Maximum (Fontana et al., 2014), near Venice, where soils formed in the past in well-drained conditions, developing a calcic horizon; the area was subsequently submerged, due to rising sea level. In the recent past, the land was reclaimed for agricultural use and the area is currently artificially drained. Soils are decarbonated in the surface horizons and have very developed calcic horizons at 70–100 cm depth; within ITA_DOG, the more clayey soils have vertic properties and they are Cambic Calcisols (Aric, Pantoclayic, Gleyic, Vertic), whereas those having less clay but equally somewhat poorly drained, are Calcaric Calcic Gleysols (Aric, Drainic, Humic, Siltic).

Within these three plots, 162 soil samples (0–30 cm) were collected in Spring 2018 using a random stratified sampling according to soil types detected within each of the three plots. Each sample is a composite one, based on 5 sub-samples taken by means of an auger, one in the middle and the other 4 subsamples collected at a distance of 5 m from the center (Fig. 2).

Samples were analyzed in the accredited ARPAV laboratory in Treviso. Particle size distribution was determined by the sieving and sedimentation method (ISO 11277:2020). Organic and inorganic carbon were determined by means of the dry combustion method in a current of oxygen using a temperature ramping program, following the draft standard CEN (prEN 17505:2020). Total SOC results from fractions released up to 600 °C, whereas inorganic carbon is the fraction released at temperatures between 600 and 900 °C.

The SOC content is quite low for the ITA_SAL dataset (from 0.51 to 0.81 %) where the soil is mainly sandy loam, while the other two sites are both characterized by an average SOC content close to 1.5 % and the soil textures are mostly silty clay (Table 3). The correlations between SOC, clay and sand content are all significant for ITA_DOG and ITA_VAL datasets, while for ITA_SAL, a significant correlation was observed only between sand and clay content (Table 3).

2.1.4. Lithuanian test sites

Three different agricultural areas were selected that fall into different agro-climatic zones (Bukantis, 2009) under humid continental climate (Dfb).

LIT_VEZ site is located in the western part of Lithuania in the Southwestern Samogitian undulating moraine plain. This location falls within the I agroclimatic zone (Bukantis, 2009), which is moderately cool and wet. The mean annual temperature of the agro-climatic zone I is 7.7 °C and annual precipitation is 910 mm (mean values over the 30 years period 1991–2020). Common soil types in the study area are Glossic Albic Eutric Retisol (Loamic, Aric, Drainic) and Epigleyic Albic Haplic Luvisol (Loamic, Aric). These soils were formed in the territorial complex of the dominant ground and supplementing marginal morainic deposits. In the sampling area, crops are grown in 3-course rotation and under conventional management intensity.

LIT_VAL site is located in the central part of Lithuania in the Nevèžis moraine plain. The selected field falls into the agro-climatic zone IID, which is moderately cool and relatively dry. The mean annual temperature of the agro-climatic zone IID is 7.5 °C and the annual precipitation is 569 mm. The soil is Endogleyic Endostagnic Endocalcaric Luvisol (Loamic). These soils were formed in the ground moraine loam deposits. In the sampling area crops are grown in 4-course crop rotation: spring barley, red clover (*Trifolium pratense L.*), winter wheat, spring wheat. Crops are grown under three levels of management intensity: conventional, integrated, and low-organic.

LIT_RUM site is located in the southwestern part of Lithuania in the Lower Nemunas limnoglacial plain. The selected field falls into the agro-climatic zone IIB, which is warm and moderately wet (Bukantis, 2009. The mean annual temperature of the agro-climatic zone IIB is 8.0 °C and the annual precipitation is 650 mm. Soil types in the study area are Endocalcaric Gleysol (Siltic, Aric, Drainic, Humic) and Epigleyic Endocalcaric Cambisol (Siltic, Aric, Drainic, Humic). These soils were formed in the limnoglacial loam deposits. In the sampling area crops are grown in 3-course rotation and under conventional management intensity.

The same sampling strategy was used in all the selected fields, i.e. we a used grid of 20 m × 20 m. Samples were taken from the depth of 0–20 cm and each sample consisted of three-four sub-samples taken within an area of 1 m radius (Fig. 2). At the sampling date (May 2021 for LIT_RUM and LIT_VEZ and September 2021 for LIT_VAL), the soil was always bare. Soil samples were air-dried and passed through different size sieves in the laboratory (2 mm size sieves for texture analyses and 0.25 mm size sieves for SOC analyses). SOC content was determined by photometric procedure at the wavelength of 590 nm using UV–VIS spectrophotometer Cary (Varian) and using glucose as a standard. Soil texture fraction was determined using the pipette method.

The three Lithuanian soil datasets have similar mean SOC content but it varies from 1 to 2.78%. The soil texture is mainly loam for LIT_VAL and LIT_VEZ and clay loam for LIT_RUM (Table 2). The correlations between SOC, clay and sand content are all significant for LIT_RUM, and LIT_VEZ datasets, while for LIT_VAL, a significant correlation, although rather low, can be observed only between SOC and sand (Table 3).

2.2. Sentinel-2 data collection

A two-years satellite data collection was selected in the Google Earth Engine (GEE) environment using the Copernicus Sentinel-2 Multi-Spectral Instrument (MSI) level 2A (from September 2019 to September 2021) within each study site. Level 2A is an operational product delivered by European Space Agency (ESA) that provides Bottom of Atmosphere (BOA) reflectance images derived from Level 1C images generated using the atmospheric correction Sen2cor processor (Main-Knorn et al., 2017). Level 2A images also provide a scene classification including cloud/snow detection, and their probability, using bands ratios and brightness thresholds. For each pixel and each acquisition date, three spectral indices were computed according to the MSI's bands (Table 4): Normalized Difference Vegetation Index (NDVI) (Eq. (1)), Normalized Burn Ratio 2 (NBR2) (Castaldi et al., 2019a) (Eq. (2)) and Bare Soil Index (BSI) (Rikimaru et al., 2002; Eq. (3)).

$$NDVI = \frac{B8 - B4}{B8 + B4} \tag{1}$$

Table 4

Number of bare soil images per year (Nb/y) for the ten tests sites obtained from the two years' Sentinel-2 time series and the most frequent months used to retrieve the synthetic bare soil images.

Site	Nb/y	maxBSI	minS2WI	Median	R90
TUR_KOC	14.7	September	September	August	October
TUR_DAL	14.0	October	October	August	October
USA_SDA	7.9	May	May	May	November
USA_MIN	28.1	April	April	May	November
ITA_SAL	13.5	July	June	June	October
ITA_DOG	13.2	July	October	June	November
ITA_VAL	12.7	March	June	June	November
LIT_RUM	1.6	April	April	June	June
LIT_VAL	7.6	September	September	March	September
LIT_VEZ	3.2	April	April	April	October

$$NBR2 = \frac{B11 - B12}{B11 + B12} \qquad (2)$$

$$BSI = \frac{(B12 + B4) - (B8 + B2)}{(B12 + B4) + (B8 + B2)} \qquad (3)$$

Since BSI was originally conceived to discriminate between bare soil and other land cover according a threshold value of 0.021 (Diek et al., 2017), a preliminary investigation was carried oud using the two Turkish sites in order to test if BSI can be used alone for bare soil selection over a Sentinel-2 time series. However, the results of the preliminary investigation highlighted failure to exclude very high NBR2 values from the time series when using only the BSI threshold, thus including areas with a high probability of the presence of non-photosynthetic vegetation according to findings by Demattê et al. (2018). Although BSI is highly negatively correlated to both NDVI and NBR2 (Fig. 3a and 3b) because its formula includes NIR, red and SWIR bands, many pixels were classified as bare soil from BSI had NBR2 values between 0.125 and 0.28 (Fig. 3b). These results suggested that the combined use of at least one of either BSI or NDVI plus NBR2 was preferable compared to the use of BSI alone. In this work, in order to carry out a stricter bare soil selection over the time series, it was decided to use all three indices as follows: excluding pixels having NDVI values higher than 0.35, NBR2 values higher than 0.125 (Castaldi et al., 2019a) and BSI < 0.021 (Diek et al., 2017). Moreover, a cloud mask was applied
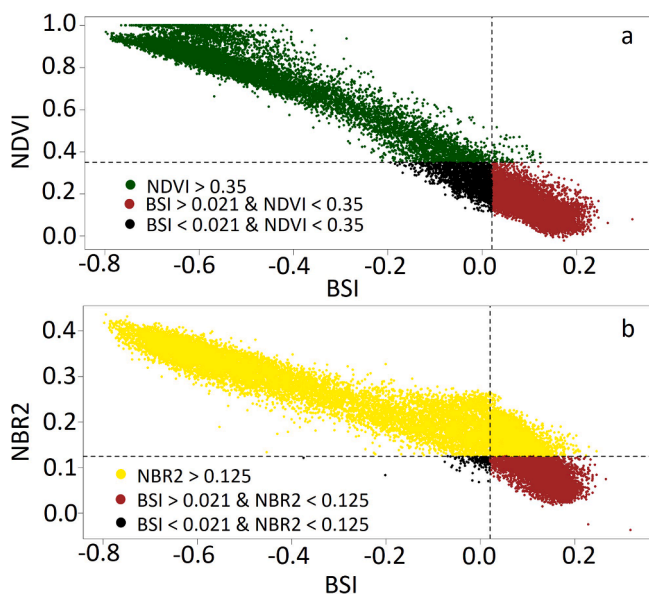
to remove regions affected by clouds using the QA60 Sentinel-2 bitmask band to mask cirrus and dense clouds obtained from Sentinel-2 Level 1C products at 60 m resolution, and mainly based on B2 reflectance threshold for dense clouds and on B10 for cirrus. While 'MSK_CLDPRB' band was used to remove clouds and clouds' shadows and 'MSK_SNWPRB' to remove snowy areas. Clouds and snow probability masks are generated by the scene classification algorithm by Sen2Cor processor.

The masking process enabled bare soil Sentinel-2 image collection for each study site (Fig. 4).

2.3. Spectral data selection

A pixel-based approach was applied to select the best bare soil conditions from the bare soil Sentinel-2 collection for each pixel falling within the study sites. Four different approaches were followed (Fig. 4): the first relies on the selection of the date showing the maximum BSI throughout the time series (hereafter referred as maxBSI) to increase the possibility of selecting pure bare soil conditions; the second approach aims to detect the driest soil conditions throughout the time series selecting the date showing the minimum soil moisture index S2WI (hereafter referred as minS2WI; Vaudour et al., 2019; Eq. (4)); the third approach entails the computation of the median reflectance value for each band (hereafter referred as Median), with the aim to obtain spectral data representative of the average bare soil conditions not affected by extreme reflectance values;

Fig. 3. scatterplots of Bare soil index (BSI) vs Normalized Vegetation Index (NDVI) (a) and BSI vs Normalized Burned Ratio 2 index (NBR2) (b) computed within the two Turkish test sites for two years' time series.
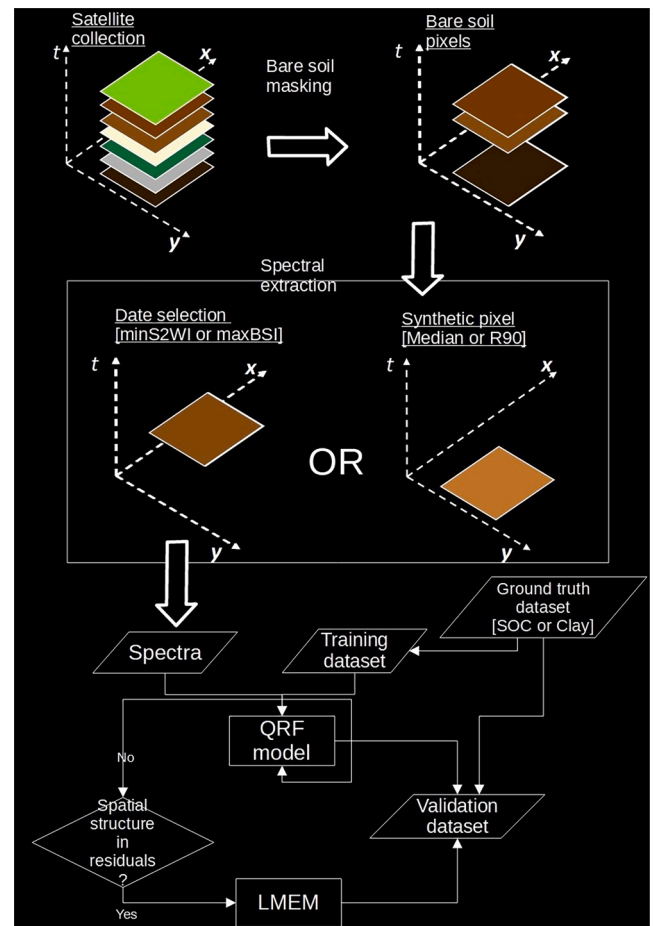
Fig. 4. Workflow showing processing scheme to obtain the bare soil composite images over the satellite time series and the calibration of prediction models for soil organic carbon and clay and their validation.

$$S2WI = \frac{B8A - B11 - B12}{B8A + B11 + B12} \qquad (4)$$

the fourth approach, called R90, aims to select dry conditions selecting the 90th percentile reflectance values throughout the time series for each band, assuming that higher reflectance correspond to lower soil moisture content. Using the 90th instead of the highest reflectance, allows to exclude anomalous data that could be detected in the final decile of the distribution mainly due to a cloud mask error. As observed in Fig. 5, the selection of the maximum reflectance values would have resulted in the selection of a cloud spectrum (blue line) due to a non-perfect functioning of the mask that, even though it could remove most cloudy pixels within the field, was not able to mask some clouds at the very sampling point highlighted in red. Whereas using the R90 spectrum results in a cloudless image acquired in June 2021, in a very droughty period in Veneto region according to the rainfall data recorded by the Environmental Protection Agency of the Veneto Region (ARPAV).

2.4. Soil properties estimation models

Each soil dataset was split into two subsets containing 80% (training dataset) and 20% (validation dataset) of the whole dataset, so they have a very similar *target variable (Y)* range. Each dataset was ordered according to the *Y* values (decreasing order) and one sample out of every five was selected for the validation dataset, and the remaining samples were used for the training dataset.

Each individual test site was modeled separately. The models calibrated on the training datasets were tested on the validation datasets for each test site. The clay and SOC contents (the target variable) of each dataset and the spectra extracted from each of the four SBSIs (covariates X) were combined to build prediction models using the Quantile Regression Forest (QRF) algorithm (Meinshausen, 2006). QRF is very

similar to the Random Forest approach, the main difference between the two is that, for QRF, all the observations are kept for each node in each tree of the forest, and not only the mean value like for random forest. Therefore, it is possible to retrieve the conditional distribution of the dependent variable, and consequently, the standard deviation and the mean value for each estimated value. Nine conditional quantiles were computed (from 0.1 to 0.9) and extracted from the estimated conditional distribution. Two kinds of QRF models were calibrated: first (QRF) using only 11 Sentinel-2 bands as covariates, the second using 11 Sentinel-2 bands plus the longitude and latitude coordinates as twelfth and thirteenth covariates (QRFxy).

For the QRF and QRFxy prediction modelling, the packages quantregForest (Meinshausen and Maintainer, 2015), randomForest (Liaw and Wiener, 2002) and caret (Kuhn, 2008) of the R software (R Core Team, 2022), were employed. The caret package allowed tuning the random forest parameters according to out-of-bag (OOB) error computation at the addition of each new tree during training process, therefore the model is fitted and tested during the training avoiding overfitting issues related to other approaches such as cross-validation. The OOB error is the average error obtained using predictions from trees not including an out-of-bag observation in their corresponding bootstrap sample.

Moreover, in order to include the spatial autocorrelation of the soil properties, whenever it is exhibited, a so-called "hybrid model" was also tested. The Linear Mixed Effect Model (LMEM) is a hybrid model that combines deterministic and stochastic approaches, i.e. regression and the spatial structure of the residuals (Odeh et al., 1995). This model allows to estimate at the same time the fixed effect coefficients β and the error covariance function parameters, the first by least squares method, and the latter by a restricted maximum likelihood (REML) method. The stochastic part of the LMEM provides information about the variance of each estimated value. The formula of the LMEM is.
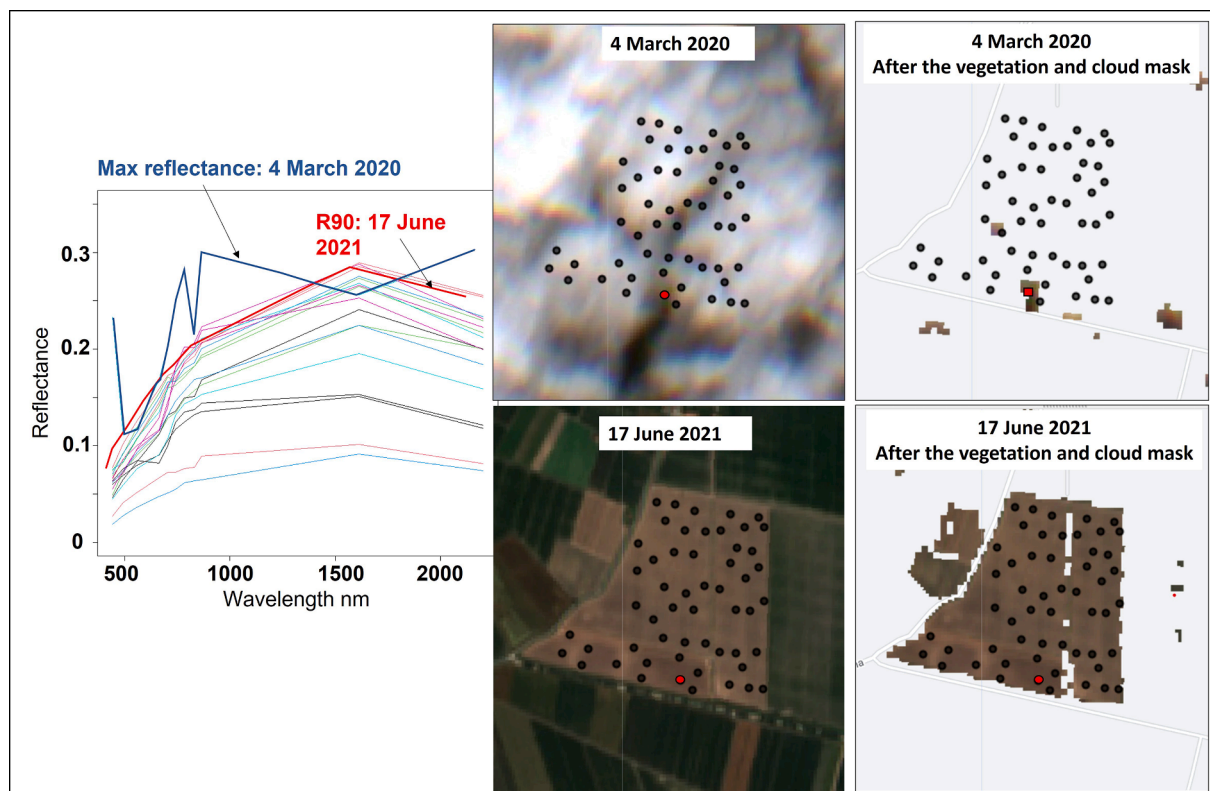
Fig. 5. Exemplification of the R90 approach for a single pixel (red point): all bare soil spectra extracted at this red point from the 2-years Sentinel-2 time-series (left); the Sentinel 2 images corresponding to the spectrum having the maximum (4 March 2020) and R90 (17 June 2021) reflectance values (right). (For interpretation of the references to colour in this figure legend, the reader is referred to the web version of this article.)

$$Y_i = X_i\beta + Z_i + \varepsilon_i \tag{5}$$

Where Y_i is the target variable at location i, X_i is the vector containing non-random covariates, β is a vector of the fixed effects coefficients, Z_i represents the spatially correlated random effects expressed by the covariance functions of the distance and described by the sill, range, and nugget effect, and ε_i is the nugget variance, thus the random error non spatially correlated.

Both prediction algorithms (QRF and LMEM) allow measuring the range of the response variable from which prediction intervals are constructed, i.e. the uncertainty of the model for each i predicted value within the test sites, which is here represented as the pixelwise ratio between standard deviation σ_i and the average estimated value $\overline{Y}_i$ of the distribution (Eq.6).

$$Uncertainty = \frac{\sigma_i}{\overline{Y}_i} \tag{6}$$

The model accuracy was assessed by computing the coefficient of determination (R²; Eq. (7)), Root Mean Square Error (RMSE; Eq. (8)), the Ratio of Performance to InterQuantile distance (RPIQ; Eq.9) and the Accuracy (Eq. (10)),

$$R^2 = 1 - \frac{\sum_i^n (Y_o - Y_p)^2}{\sum_i^n (\overline{Y} - Y_p)^2} \tag{7}$$

$$RMSE = \sqrt{\frac{\sum_i^n (Y_o - Y_p)^2}{n}} \tag{8}$$

$$RPIQ = \frac{IQ}{RMSE} \tag{9}$$

$$Accuracy = \frac{\sum_i^n 100 - \left(\frac{|Y_o - Y_p|}{Y_o} * 100\right)}{n} \tag{10}$$

with Y_o as the observed values in the validation datasets, Y_p the predicted values, $\overline{Y}$ the average observed value, n the number of observations in each validation dataset and IQ the interquartile range.

Andries et al. (2021) indicated a required level of accuracy for monitoring organic carbon stocks in the soils by EO-based techniques using a semi-quantitative metric based on interviews, i.e. how much EO-based estimated values should match those retrieved by "traditional" approaches (soil sampling plus laboratory analysis) to be considered efficient. Therefore, Equation (10) was conceived to make mathematically explicit the accuracy levels showed in Andries et al. (2021).

For the QRF and QRFxy models, the increase in mean square error (Inc_MSE) of prediction, estimated with out-of-bag cross-validation, was computed for each covariate. The Inc_MSE values were obtained as the average difference between MSE of prediction before and after permuting each covariate and normalized by standard deviation. The Variable Importance (VI) are shown as Inc_MSE standardized by minimum and maximum values of all covariates to have scores between 0 and 1. For LMEM, the mean fixed effect coefficient β of each covariate X was normalized by its standard deviation and standardized by minimum and maximum values in order to obtain VI values between 0 and 1. For both QRF and LMEM, the higher the VI value, the more important the covariate.

3. Results

3.1. Synthetic bare soil images – SBSI

The average number of bare soil conditions for each pixel per year (Table 4) was the highest for USA_MIN (28.1), while the lowest frequencies were observed for the Lithuanian sites, and in particular for the LIT_RUM and LIT_VEZ fields for which the frequency was close to 2 and 3 respectively. The frequency was high and ranged between 12.7 and 14.7 for all Mediterranean sites (Türkiye and Italy).

The four different spectral data selection approaches allowed to obtain the SBSIs shown in Fig. 6. Spectral data were extracted at the soil sampling locations from all four SBSIs. Since the SBSIs were mosaicked using images acquired at different dates, the most frequent month per spectral data selection approach at each site was reported in Table 4. Similar results can be observed comparing maxBSI and minS2WI, with autumnal images in Türkiye, spring in USA, and summer in Italy. For the Lithuanian test sites, April was the most common month for LIT_VEZ and LIT_RUM, while for LIT_VAL this was September. The Median approach provided different results as compared to the first two approaches, especially for Turkish sites where August data were more frequent and for LIT_VAL where the spectral data were mainly retrieved from March images. The R90 approach mostly used data acquired in autumn whatever site except for LIT_RUM.

Observing the SBSIs images, the maxBSI and minS2WI selection produced a spotty composite in some sites: this effect was particularly noticeable for USA_SDA and USA_MIN (Fig. 6b) and for all the Lithuanian (Fig. 6c) and Italian sites (Fig. 6d).

3.2. SOC and clay prediction accuracy

3.2.1. Validation results for sites

Prediction performances varied according to sites, SBSIs and models. The best predicted sites for SOC were those showing the highest SOC range, higher than 1.8% (USA_MIN, USA_SDA, LIT_RUM). The best predicted sites for clay are among those having a substantial range higher than 26%, relying on within field contrasting soil types from Fluvisols to Vertisols (51%, TUR_KOC), Chernozem to Gleysols (USA_SDA), Gleysols to Calcisols (ITA_VAL).

For half of the sites, the best SBSI for SOC was the Median SBSI: for TUR_DAL and LIT_VEZ, minS2WI yielded the highest accuracy, while for LIT_VAL R90 allowed to obtain the best performances (Table 5). The highest RPIQ values for each site ranged between 1.45 (LIT_VEZ) and 6.14 (USA_SDA) and higher accuracies were generally obtained taking the spatial autocorrelation into account, i.e. using QRFxy or LMEM.

The R90 yielded the best validation accuracy for 4 out of 10 sites for clay: namely for both Turkish sites, for USA_MIN and ITA_DOG. Models using Median data showed best performances for ITA_VAL and LIT_VEZ, maxBSI for ITA_SAL and LIT_RUM and minS2WI for USA_SDA. The best statistics for each site, in terms of RPIQ value, were slightly lower as compared to those observed for SOC and ranged between 1 (LIT_VAL) and 6.99 (USA_SDA).

As some best predicted sites had a sampling density as low as 0.3 or 0.4 samples per hectare, the sampling density does not seem to influence the prediction performance.

The Accuracy values higher than 90% were highlighted in bold in Table 5: this threshold corresponds to the required accuracy from EO-based techniques to monitor and reporting organic carbon stocks in the soils (Andries et al., 2021). The same accuracy threshold was here adopted for clay estimation. Table 6 and 7 shows the frequency of Accuracy values higher than 90% in Table 5, respectively for SOC and clay estimation. For SOC estimation the most performing SBSI is R90 (53%), and more than half of the QRFxy models provided an Accuracy higher than 90% (Table 6). Consequently, the best combination of SBSI and model are Median_QRFxy and R90_QRFxy. The frequency of Accuracy >90% is generally low for clay as compared to SOC (Table 7); Median and R90 provided the highest frequency, and QRFxy and LMM models are generally more accurate than QRF, especially in combination with R90.

3.3. VI analysis

The average VI score among the ten sites for each band and its standard error are shown in Figs. 7 and 8. The VI analysis highlights the importance of longitude (X) and latitude (Y) as covariates in the QRFxy
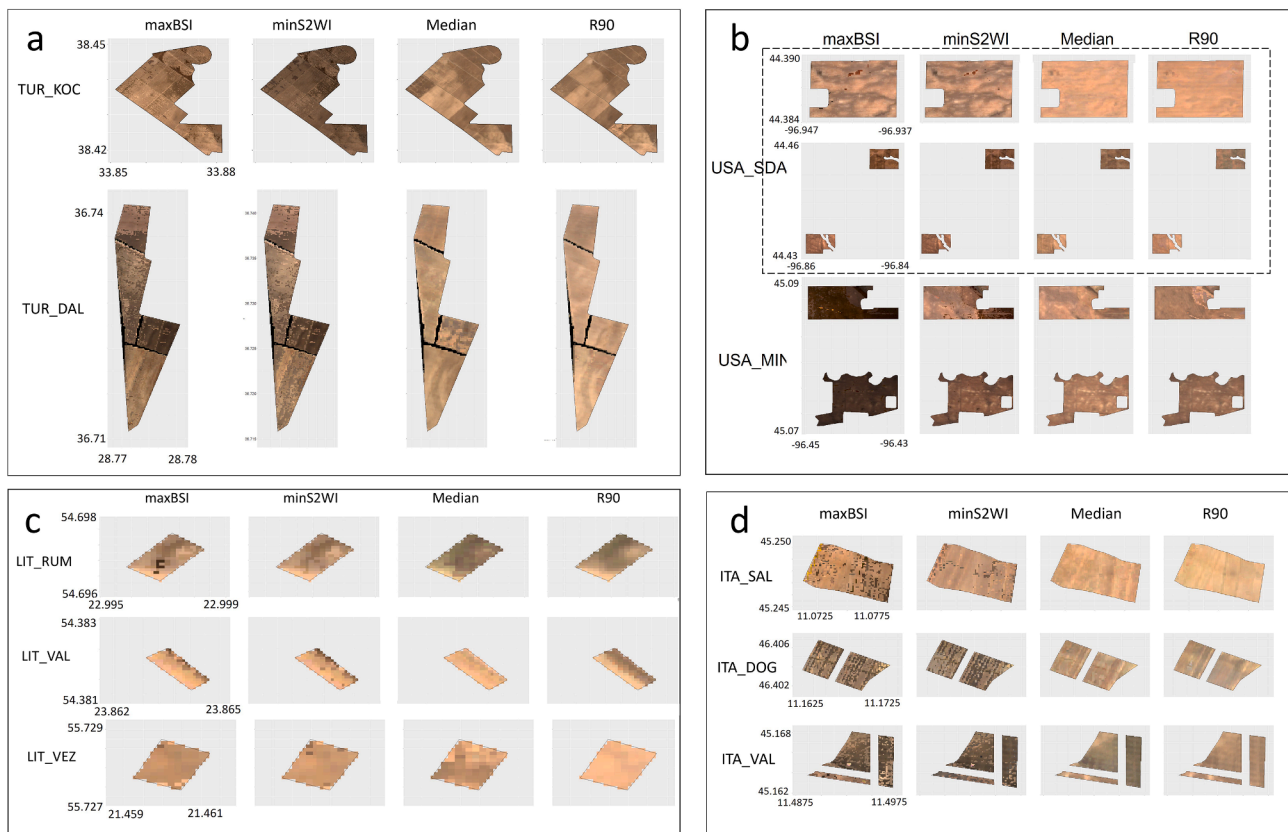
Fig. 6. Synthetic bare soil images obtained in the Turkish (a), USA (b), Lithuanian (c) and Italian (d) sites using the two years' Sentinel-2 time series.

models for SOC prediction using all the four composite images (SBSI) (Fig. 7). For SOC estimation, the most important band was B12, especially for the models calibrated using Median and R90 data. Concerning QRF models, apart from B11 and B12, no substantial differences could be detected among the other bands for minS2WI, maxBSI and R90 data, while for the Median SBSI, the bands B2 and B4 showed high VI values and B8 the lowest importance. For the calibration of LMEMs, the NIR bands, B2, and B11 had the highest VI values.

For clay estimation, by QRFxy models the most important covariates were X, Y and B12 (Fig. 8). B12 is still very important for QRF, for which high VI scores were also detected for B2, B8 and B11 using Median data. The VI values retrieved from LMEMs showed low values for B3, B6 and B12 for most of the SBSIs, while the other bands showed small differences among them in terms of VI values.

In general, all the VI values exhibited high variability among the ten sites.

3.4. Uncertainty of predicted values

QRF models and maxBSI data were excluded from the uncertainty analysis due to the low prediction accuracy highlighted in Table 5. The uncertainty was computed both for the validation dataset and for the soil property maps, therefore for all the other pixels within the selected fields.

Although the uncertainty of the predicted values of the validation datasets is similar between QRFxy and LMEM (data not shown), relevant differences exist between these two models in terms of the uncertainty of the soil property maps, especially for clay (Table 8). In general, LMEMs lead to higher uncertainty, also where they provided the best validation performances. For example. for TUR_KOC, even though Median + LMEM had the highest RPIQ (Table 5), the average uncertainty was really high (0.46). The QRFxy models provided a very similar average uncertainty between SBSIs, both for SOC and clay, ranging from 0.12

and 0.145, while the average uncertainty values for LMEMs ranged from 0.13, for SOC model using R90, to 0.82 for clay estimation using minS2WI.

3.5. SOC and clay mapping

The QRFxy and LMEMs were applied to minS2WI, Median and R90 SBSIs to obtain SOC and clay maps at six of the test sites deemed representative of the climate and soil types investigated in the present work (TUR_KOC, TUR_DAL, USA_SDA, USA_MIN, ITA_VAL and LIT_RUM) and the associated uncertainty maps.

The differences in terms of estimation and uncertainty between QRFxy and LMEM for TUR_KOC site are reflected in the SOC (Fig. 9a and 9b) and clay (Fig. 9c and 9d) maps. The patterns of the SOC maps obtained by QRFxy are consistent with those observed in Median and R90 SBSIs (Fig. 5a), while LMEM provided less clear SOC patterns across the TUR_KOC fields and very large uncertainty all over the site (Fig. 9b). Both clay maps, the one obtained from QRFxy (Fig. 9c) and the one gained from LMEM (Fig. 9d), showed a large uncertainty, however, combining R90 and LMEM, it was possible to get the best validation accuracy and clay patterns that reflect those detectable within the temporal mosaics.

The SBSIs made for the USA_SDA site using minS2WI approach look spotted, and this characteristic affected the reliability of the soil properties maps as shown in Fig. 10 where minS2WI + QRFxy and Median + QRFxy models are compared. The Median SBSI allowed to make SOC and clay with clear patterns within the field, highlighting the spatial variability of both soil properties, and significantly reducing the uncertainty (Fig. 10b and 10d) as compared to the results obtained by minS2WI data (Fig. 10a and 10c).

The best models according to Table 5 statistics were used to make the SOC and clay maps depicted respectively in Figs. 11 and 12.

Table 5

Validation results of the soil organic carbon (SOC) and clay prediction models for each test site. The statistics used area: R^2 = coefficient of determination; RMSE = root mean square error; RPIQ: ratio of performance to interquartile range. SBSI = synthetic bare soil image; Acc. = accuracy.

Site	SBSI	Model	SOC R^2	RMSE %	RPIQ	Acc. %	Clay R^2	RMSE %	RPIQ	Acc. %
TUR_KOC	maxBSI	QRF	0.05	0.23	1.22	83.1	0.33	9.61	1.78	80.4
		QRF_XY	0.43	0.18	1.60	86.1	0.30	9.88	1.73	80.3
		LMM	0.43	0.18	1.54	85.4	0.54	8.04	2.13	84.4
	minS2WI	QRF	0.00	0.24	1.18	81.8	0.50	8.01	2.13	83.9
		QRF_XY	0.42	0.18	1.59	85.6	0.50	8.07	2.12	84.6
		LMM	0.53	0.16	1.72	86.3	0.50	9.06	1.89	81.5
	Median	QRF	0.16	0.22	1.31	84.1	0.61	7.24	2.36	85.8
		QRF_XY	0.57	0.15	1.84	88.1	0.64	6.99	2.45	86.7
		LMM	0.61	0.15	1.94	88.2	0.59	7.70	2.22	86.5
	R90	QRF	0.26	0.20	1.40	83.9	0.64	7.32	2.34	86.1
		QRF_XY	0.59	0.15	1.85	88.2	0.60	7.60	2.25	85.7
		LMM	0.47	0.18	1.57	85.8	0.78	6.14	2.79	87
TUR_DAL	maxBSI	QRF	0.45	0.14	1.78	85.1	0.30	7.11	1.18	85.3
		QRF_XY	0.59	0.12	2.06	87.4	0.65	5.35	1.58	80.8
		LMM	0.75	0.09	2.59	**91.0**	0.47	6.43	1.31	86.0
	minS2WI	QRF	0.21	0.16	1.51	86.0	0.22	7.25	1.16	82.6
		QRF_XY	0.62	0.11	2.14	87.2	0.75	5.05	1.67	82.1
		LMM	0.75	0.09	2.72	**91.8**	0.56	5.85	1.44	84.1
	Median	QRF	0.37	0.15	1.68	85.0	0.32	6.71	1.26	83.8
		QRF_XY	0.53	0.12	1.97	87.0	0.63	5.12	1.65	84.7
		LMM	0.79	0.09	2.61	89.8	0.55	5.69	1.48	87.2
	R90	QRF	0.65	0.11	2.27	**90.3**	0.32	6.80	1.24	85.0
		QRF_XY	0.69	0.10	2.39	**90.4**	0.54	5.51	1.53	79.4
		LMM	0.56	0.13	1.96	88.0	0.70	4.57	1.84	88.0
USA_SDA	maxBSI	QRF	0.7	0.38	2.57	89.2	0.92	2.78	6.31	89.7
		QRF_XY	0.9	0.22	4.53	**92.4**	0.9	3.03	5.78	89.2
		LMM	0.79	0.31	3.16	87.4	0.9	3.26	5.38	**90.2**
	minS2WI	QRF	0.88	0.23	4.27	**91.9**	0.93	2.63	6.68	**90.3**
		QRF_XY	0.94	0.16	6.07	**93.9**	0.94	2.51	6.99	**91.1**
		LMM	0.88	0.24	4.14	90.7	0.9	3.47	5.06	87.1
	Median	QRF	0.8	0.35	2.77	86.5	0.93	2.71	6.49	88.7
		QRF_XY	0.96	0.16	6.14	**93.9**	0.91	3	5.85	89.3
		LMM	0.76	0.34	2.85	88.1	0.88	3.49	5.03	85.3
	R90	QRF	0.94	0.18	5.47	**94.4**	0.83	4.44	3.95	86.2
		QRF_XY	0.96	0.17	5.82	**94.4**	0.9	3.2	5.48	88.5
		LMM	0.89	0.24	4.03	**92.2**	0.83	4.28	4.11	84.8
USA_MIN	maxBSI	QRF	0.57	0.34	1.77	89.9	0.33	4.58	1.55	89.2
		QRF_XY	0.56	0.34	1.77	90.2	0.33	4.64	1.53	87.7
		LMM	0.19	0.45	1.32	84.8	0.36	5.51	1.29	85.1
	minS2WI	QRF	0.75	0.26	2.29	**90.8**	0.22	4.97	1.43	88.3
		QRF_XY	0.71	0.28	2.16	90.6	0.33	4.59	1.55	87.9
		LMM	0.62	0.3	1.98	89.8	0.55	4.89	1.45	87.5
	Median	QRF	0.69	0.32	1.9	**90.1**	0.16	5.13	1.38	87.1
		QRF_XY	0.8	0.26	2.31	**91.9**	0.38	4.45	1.59	88.0
		LMM	0.75	0.24	2.47	**92.4**	0.69	4.18	1.7	89.2
	R90	QRF	0.6	0.34	1.78	88.9	0.38	4.46	1.59	89.1
		QRF_XY	0.6	0.33	1.79	89.5	0.38	4.42	1.6	89.1
		LMM	0.54	0.34	1.77	89.6	0,,65	3.61	1.96	**90.7**
ITA_SAL	maxBSI	QRF	0.16	0.06	1.46	**91.8**	0.20	1.63	1.34	**90.1**
		QRF_XY	0.05	0.06	1.36	**91.3**	0.49	1.36	1.61	**91.3**
		LMM	0.02	0.1	0.87	**91.6**	0.48	1.27	1.74	**92.2**
	minS2WI	QRF	0	0.06	1.33	**91.1**	0.04	1.77	1.24	89.1
		QRF_XY	0.16	0.06	1.48	**92.1**	0.27	1.54	1.43	90.9
		LMM	0.19	0.07	1.37	**91.2**	0.13	1.96	1.12	88.8
	Median	QRF	0.17	0.06	1.45	**92.0**	0.00	1.79	1.23	88.7
		QRF_XY	0.22	0.06	1.52	**92.2**	0.34	1.45	1.51	**91.5**
		LMM	0.52	0.05	1.87	**93.2**	0.37	1.67	1.31	89.7
	R90	QRF	0.31	0.06	1.58	**93.2**	0.13	1.67	1.32	89.2
		QRF_XY	0.32	0.05	1.6	**93.2**	0.43	1.34	1.64	**90.9**
		LMM	0.36	0.05	1.64	**92.3**	0.30	1.55	1.42	**91.2**
ITA_DOG	maxBSI	QRF	0.08	0.25	1.23	85.9	0.20	6.26	1.40	85.9
		QRF_XY	0.11	0.26	1.17	85.4	0.31	5.85	1.50	87.2
		LMM	0.02	0.28	1.1	84.0	0.47	5.59	1.57	86.1
	minS2WI	QRF	0.07	0.231	1.32	87.0	0.45	5.05	1.74	88.3
		QRF_XY	0.08	0.24	1.28	86.4	0.34	5.60	1.57	87.6
		LMM	0.15	0.22	1.41	87.6	0.63	8.71	1.01	79.5
	Median	QRF	0.21	0.21	1.48	87.6	0.44	5.30	1.66	87.6
		QRF_XY	0.21	0.21	1.46	88.8	0.44	5.21	1.69	88.4
		LMM	0.57	0.16	1.88	**90.5**	0.70	4.91	1.79	88.5
	R90	QRF	0.42	0.18	1.71	**90.2**	0.52	4.67	1.88	89.8
		QRF_XY	0.46	0.17	1.77	**91.1**	0.54	4.66	1.89	**90.1**

Table 5 (*continued*)

					SOC			Clay		
		LMM	0.47	0.17	1.8	**91.5**	0.35	5.80	1.52	85.5
ITA_VAL	maxBSI	QRF	0.019	0.24	1	86.7	0.03	7.32	0.90	85.7
		QRF_XY	0.22	0.18	1.31	**90.7**	0.13	7.24	0.91	87.7
		LMM	0.18	0.21	1.11	86.9	0.27	6.01	1.10	87.3
	minS2WI	QRF	0.14	0.19	1.23	86.4	0.75	4.29	1.54	**90.6**
		QRF_XY	0.32	0.17	1.39	**91.7**	0.14	8.77	0.75	87.4
		LMM	0	0.36	0.65	79.3	0.45	6.37	1.04	88.0
	Median	QRF	0.41	0.16	1.45	**90.3**	0.73	3.32	2.02	**93.0**
		QRF_XY	0.53	0.13	1.69	**91.9**	0.80	2.86	2.35	**93.8**
		LMM	0.47	0.16	1.41	89.6	0.73	3.44	1.95	**92.6**
	R90	QRF	0.03	0.23	1.02	85.2	0.78	3.62	1.82	**92.2**
		QRF_XY	0.21	0.18	1.29	**90.3**	0.28	6.75	0.98	89.8
		LMM	0.41	0.17	1.37	**91.3**	0.74	3.72	1.77	**92.5**
LIT_RUM	maxBSI	QRF	0.62	0.26	2.34	87.6	0.51	3.91	1.77	88.8
		QRF_XY	0.64	0.26	2.41	87.6	0.62	3.60	1.92	89.7
		LMM	0.84	0.18	3.39	**90.1**	0.18	5.63	1.22	85.4
	minS2WI	QRF	0.66	0.26	2.39	87.5	0.23	4.82	1.43	86.2
		QRF_XY	0.68	0.25	2.46	87.7	0.28	4.62	1.49	87.0
		LMM	0.71	0.24	2.61	88.3	0.25	5.15	1.34	86.4
	Median	QRF	0.92	0.16	3.30	**93.6**	0.34	3.99	1.33	**91.1**
		QRF_XY	0.94	0.17	3.24	**92.9**	0.39	3.84	1.38	**91.3**
		LMM	0.42	0.39	1.40	77.3	0.43	4.35	1.22	**90.1**
	R90	QRF	0.77	0.21	2.95	89.6	0.59	4.06	1.70	89.5
		QRF_XY	0.76	0.21	2.93	89.4	0.69	3.68	1.87	**90.9**
		LMM	0.61	0.28	2.19	86.5	0.54	3.79	1.82	**90.4**
LIT_VAL	maxBSI	QRF	0.01	0.23	1.03	89.3	0.18	2.17	1.07	88.2
		QRF_XY	0.50	0.21	1.33	89.9	0.17	2.24	1.00	87.2
		LMM	0.66	0.19	1.45	88.4	0.04	2.83	0.79	81.7
	minS2WI	QRF	0.09	0.20	1.17	**91.2**	0.02	2.36	0.99	82.5
		QRF_XY	0.87	0.15	1.90	**92.3**	0.12	2.29	0.98	85.9
		LMM	0.73	0.15	1.88	**91.5**	0.17	2.81	0.80	83.4
	Median	QRF	0.26	0.19	1.32	89.7	0.03	3.32	0.78	77.1
		QRF_XY	0.36	0.18	1.38	**90.3**	0.05	3.33	0.77	76.9
		LMM	0.05	0.26	0.95	86.3	0.26	4.18	0.62	73.8
	R90	QRF	0.04	0.21	1.13	**90.1**	0.02	2.36	0.98	87.6
		QRF_XY	0.78	0.17	1.65	**90.1**	0.16	2.48	0.91	86.4
		LMM	0.76	0.15	1.91	**92.1**	0.00	2.67	0.84	84.8
LIT_VEZ	maxBSI	QRF	0.02	0.25	1.23	87.2	0.41	1.79	1.70	86.6
		QRF_XY	0.03	0.28	1.09	87.4	0.52	1.75	1.75	86.4
		LMM	0.01	0.27	1.14	86.4	0.47	1.84	1.66	87.7
	minS2WI	QRF	0.19	0.21	1.45	**90.2**	0.63	1.60	1.91	89.3
		QRF_XY	0.03	0.28	1.09	87.4	0.52	1.75	1.75	86.4
		LMM	0.09	0.32	0.95	85.3	0.64	1.50	2.04	89.8
	Median	QRF	0.02	0.27	1.10	87.6	0.64	1.64	1.87	86.6
		QRF_XY	0.03	0.28	1.09	87.4	0.52	1.75	1.75	86.4
		LMM	0.01	0.41	0.73	82.4	0.71	1.40	2.19	89.8
	R90	QRF	0.08	0.23	1.33	88.2	0.47	1.82	1.67	86.0
		QRF_XY	0.03	0.28	1.09	87.4	0.48	1.77	1.73	85.8
		LMM	0.26	0.22	1.42	89.1	0.16	2.31	1.32	85.5

Table 6

Frequency of Accuracy values higher than 90% for SOC estimation among the ten test sites according to synthetic bare soil images method (SBSI) and prediction models.

	maxBSI	minS2WI	Median	R90	Mean frequency
QRF	10%	50%	40%	50%	37.5%
QRFxy	40%	50%	60%	60%	52.5%
LMM	30%	40%	30%	50%	37.5%
Mean frequency	26.7%	46.7%	43.3%	53.3%	

Table 7

Frequency of Accuracy values higher than 90% for clay estimation among the ten test sites according to synthetic bare soil images method (SBSI) and prediction models.

	maxBSI	minS2WI	Median	R90	Mean frequency
QRF	10%	20%	20%	10%	15%
QRFxy	10%	20%	30%	30%	22.5%
LMM	20%	0%	20%	40%	20.0%
Mean frequency	13.3%	13.3%	23.3%	26.7%	

4. Discussion

We collected a dataset of very detailed spatial information at field or farm scales, for cropland sites of contrasted climates and soil types across the Northern hemisphere. Through several two-years-Sentinel-2 temporal mosaics or SBSIs, Sentinel-2 based approaches appear effective for the detailed mapping of topsoil clay and SOC contents at the local scale, yet with differences in both accuracy and uncertainties which are not all compatible with carbon monitoring. Even though prediction performance was reasonably accurate (RPIQ $\geq$ 1.8) for most sites, the results shown here highlighted how the model and SBSI selection can affect the accuracy and the uncertainty of the SOC and clay estimates. The output maps were not of comparable quality and uncertainty depending on the considered site, the SBSI, and the prediction model carried out. As this approach relies on spectral characteristics of bare soil condition, it is dependent on the availability of clear sky images as well as the occurrence of favorable soil surface conditions. The multitemporal approaches proposed and tested in this work were meant to optimize the bare soil selection, by selecting not only bare soils, but also the driest and/or the least covered by dry residues.
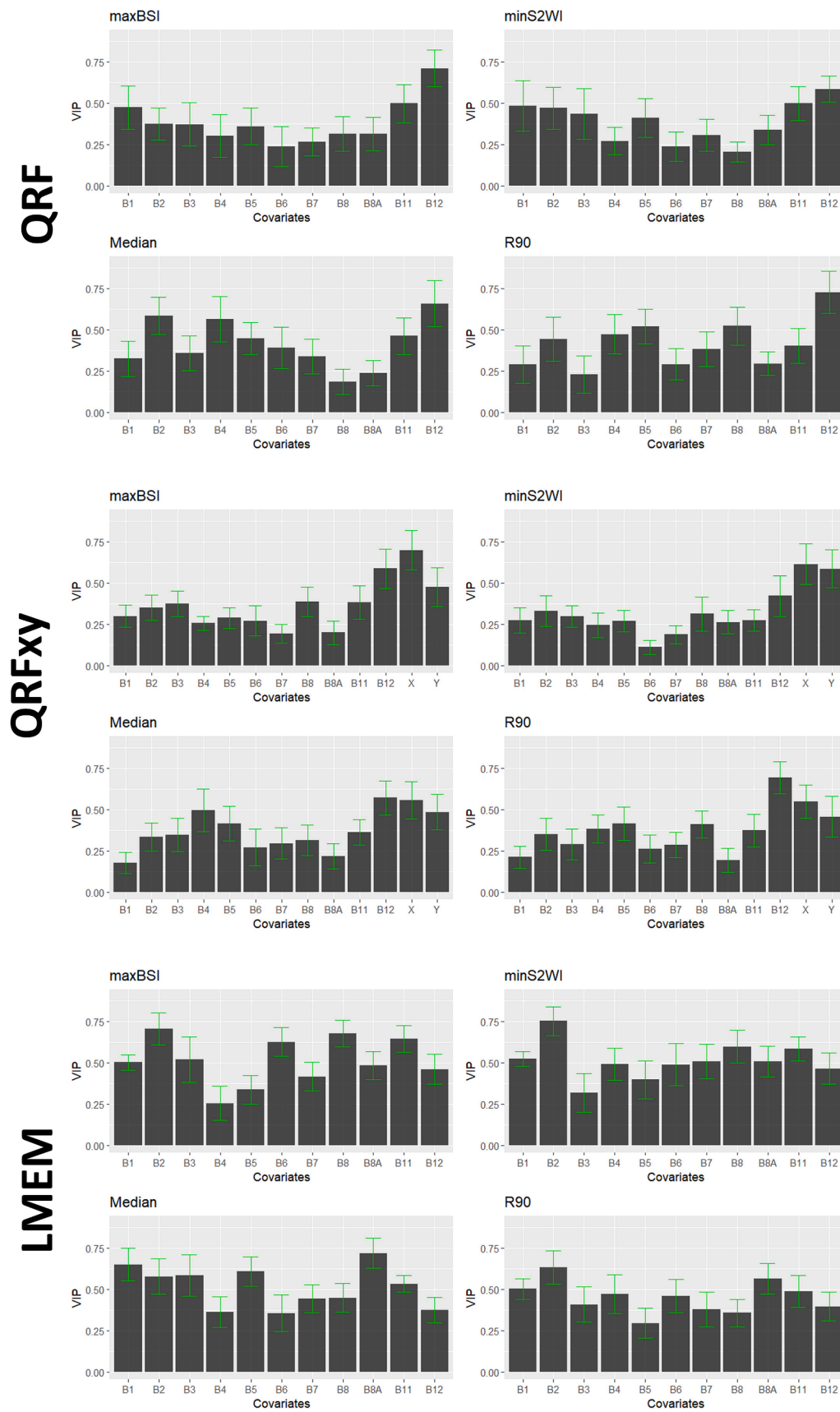
Fig. 7. Barplots showing the average variable of importance in projection (VI) values for soil organic carbon prediction models and their standard error (in green) among the ten sites. (For interpretation of the references to colour in this figure legend, the reader is referred to the web version of this article.)
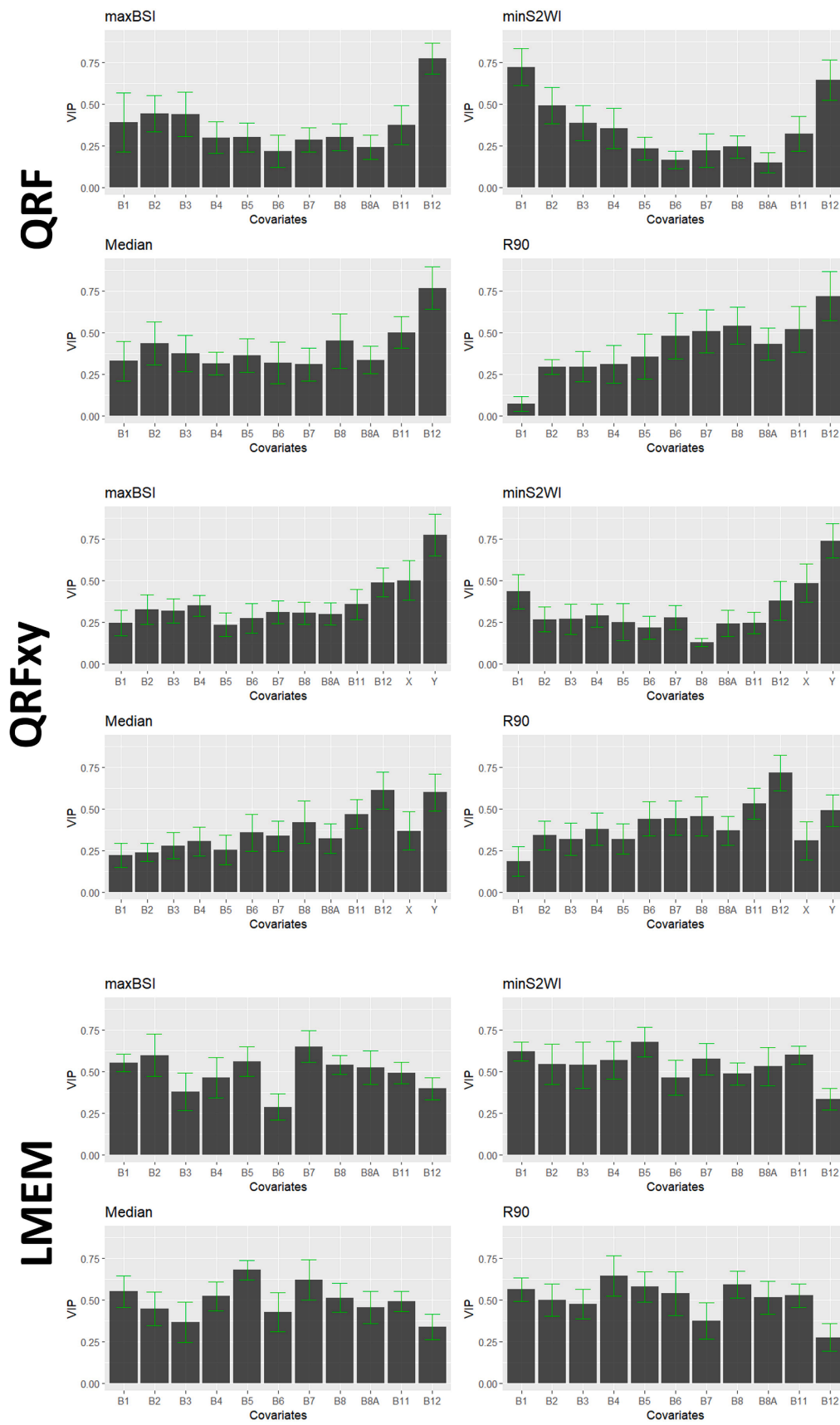
Fig. 8. Barplots showing the average variable of importance in projection (VI) values for clay prediction models and their standard error (in green) among the ten sites. (For interpretation of the references to colour in this figure legend, the reader is referred to the web version of this article.)

Table 8
Average uncertainty of the soil organic carbon (SOC) and clay predicted values within the test sites.

		minS2WI		Median		R90	
		QRFxy	LMEM	QRFxy	LMEM	QRFxy	LMEM
SOC	TUR_KOC	0.11	0.23	0.11	0.46	0.11	0.22
	TUR_DAL	0.20	0.16	0.22	0.15	0.14	0.15
	USA_SDA	0.13	0.09	0.07	0.14	0.10	0.08
	USA_MIN	0.12	0.19	0.17	0.17	0.12	0.08
	ITA_VAL	0.13	0.11	0.09	0.80	0.09	0.12
	LIT_RUM	0.13	0.77	0.14	0.11	0.13	0.12
	Mean	**0.14**	**0.26**	**0.13**	**0.31**	**0.12**	**0.13**
Clay	TUR_KOC	0.11	0.40	0.18	0.80	0.11	0.75
	TUR_DAL	0.20	1.55	0.22	0.35	0.14	0.002
	USA_SDA	0.23	0.22	0.07	1.15	0.21	0.23
	USA_MIN	0.11	1.60	0.13	1.55	0.13	1.45
	ITA_VAL	0.08	0.71	0.08	0.05	0.08	0.45
	LIT_RUM	0.14	0.45	0.18	0.11	0.13	0.15
	Mean	**0.145**	**0.82**	**0.14**	**0.67**	**0.13**	**0.51**

4.1. Differences in cloudless available frequency

The temporal mosaicking approaches tested in this work allowed as a first result to select Sentinel-2 acquisition days affected by bare soil condition, thus excluding images acquired during the vegetation growing season and those acquired when non-photosynthetic vegetation was on the field. Although the availability of bare soil conditions can vary according to farm management, the frequency of cloudy days is a really impacting factor (Li et al., 2022). As already highlighted by Castaldi (2021), the availability of bare soil images in Northern Europe is lower than in the Mediterranean region, both using Landsat 8 and Sentinel-2 collections, particularly in Ireland and the Baltic States. The cloud-free - bare soil frequency observed in the present work for the Lithuanian sites is very low and it ranges between 1.6 and 7.6 available

images per year, while an average of 13 useful images per year were detected for the Italian and Turkish sites (Table 4). This difference between the Baltic and Mediterranean areas is mainly due to the higher cloudiness in the Baltic region, the study by Paszkuta et al. (2019) estimated average annual cloudiness of around 58.5% for the Baltic sea, which can be a good indicator of inland cloudiness of the Baltic states.

4.2. Accounting for the bare soil availability periods

Farm management plays a key role, not only in the availability of bare soil images, but also in both the dynamics of SOC and the spectral properties of soil surface, the latter being influenced by fertilization and amendment practices, tillage depth and frequency, crop rotation, intermediate crops and residue management (Vaudour et al., 2022). Practices such as reduced or no tillage and legume cover crops can lead to an increase in SOC sequestration rates (Chen et al., 2015; Minasny et al., 2017) and avoiding soil erosion, especially in vulnerable areas, but they involve almost continuous ground cover. According to the *Evaluation support study on the impact of the CAP on sustainable management of the soil: final report* (European Commission, 2021), Agri-Environment and Climate Measures (AECM) were programmed in all the Member States to implement land use and management practices relevant to contribute to soil quality. Among the indicated practices in the AECM are soil cover, and reduced or no tillage.

The percentage of arable lands under AECM supporting soil cover and low tillage and conservation agriculture is still low in most European states, or even not already programmed. Conventional tillage which is practiced in 74.4% of the arable lands in the European Union group of 28 member states (EU-28) is still the most widespread tillage practice in Europe (Panagos et al., 2015), while reduced and conservation tillage covers 21.6% of the arable areas and no-tillage is applied over 4% only. Although the availability of bare soil data acquired by satellites is expected to decrease in the future, the multitemporal approaches proposed and tested in this work optimized the bare soil
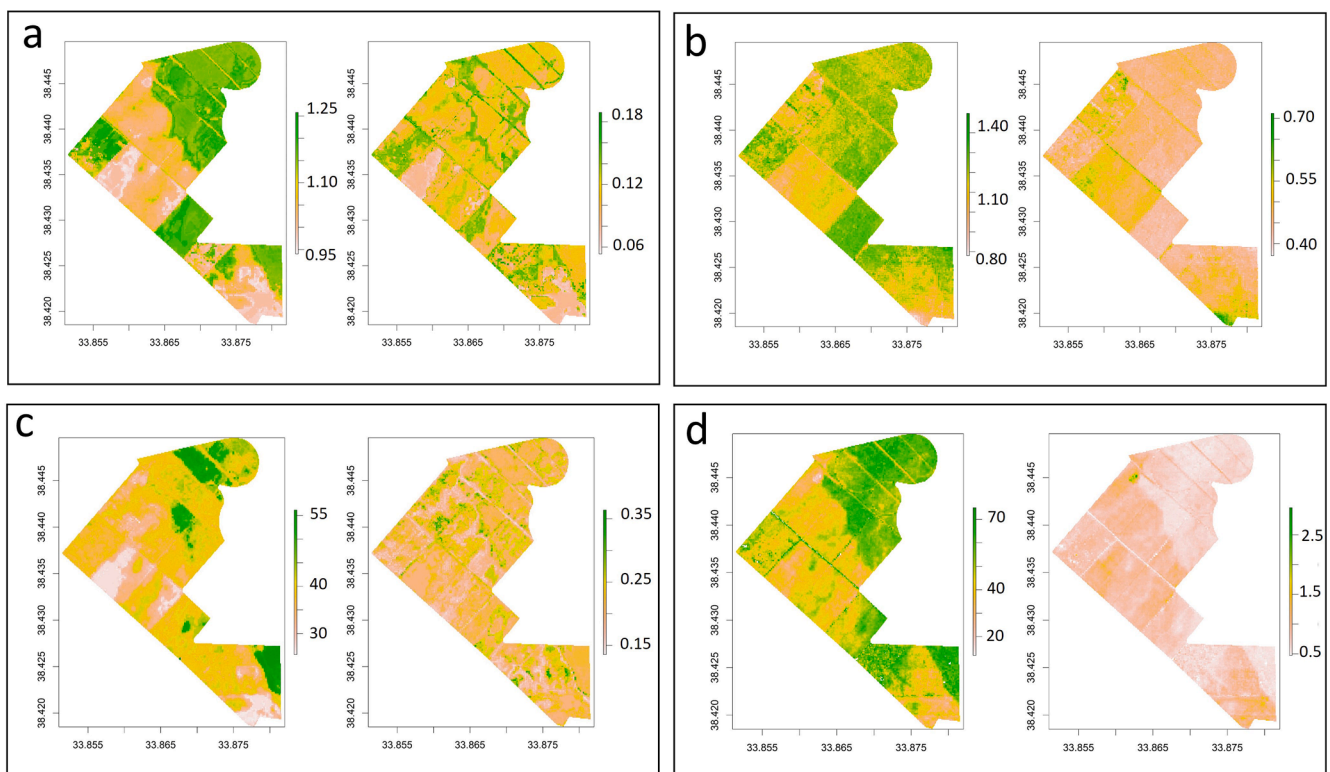

Fig. 9. Top row shows SOC and uncertainty maps obtained combing QRFxy and R90 (a) and LMEM and Median (b) for the TUR_KOC site. The bottom row shows clay and uncertainty maps obtained combining QRFxy and Median (c) and LMEM and R90 (d) for the TUR_KOC site.
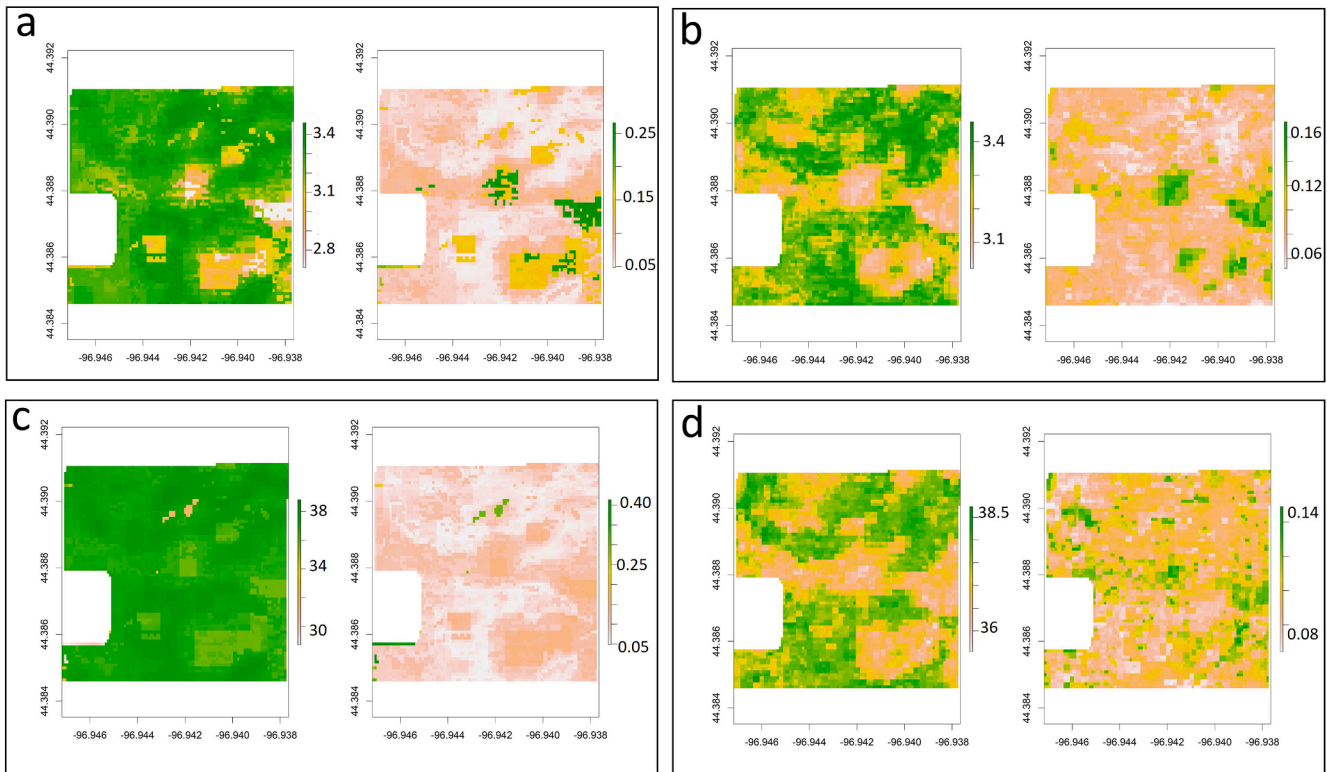
Fig. 10. Top row shows SOC and uncertainty maps obtained combining minS2WI and QRFxy (a) and Median and QRFxy (b). The bottom row shows clay and uncertainty maps obtained combining minS2WI and QRFxy (c) and Median and QRFxy (d) for one of the three fields on the USA_SDA site.
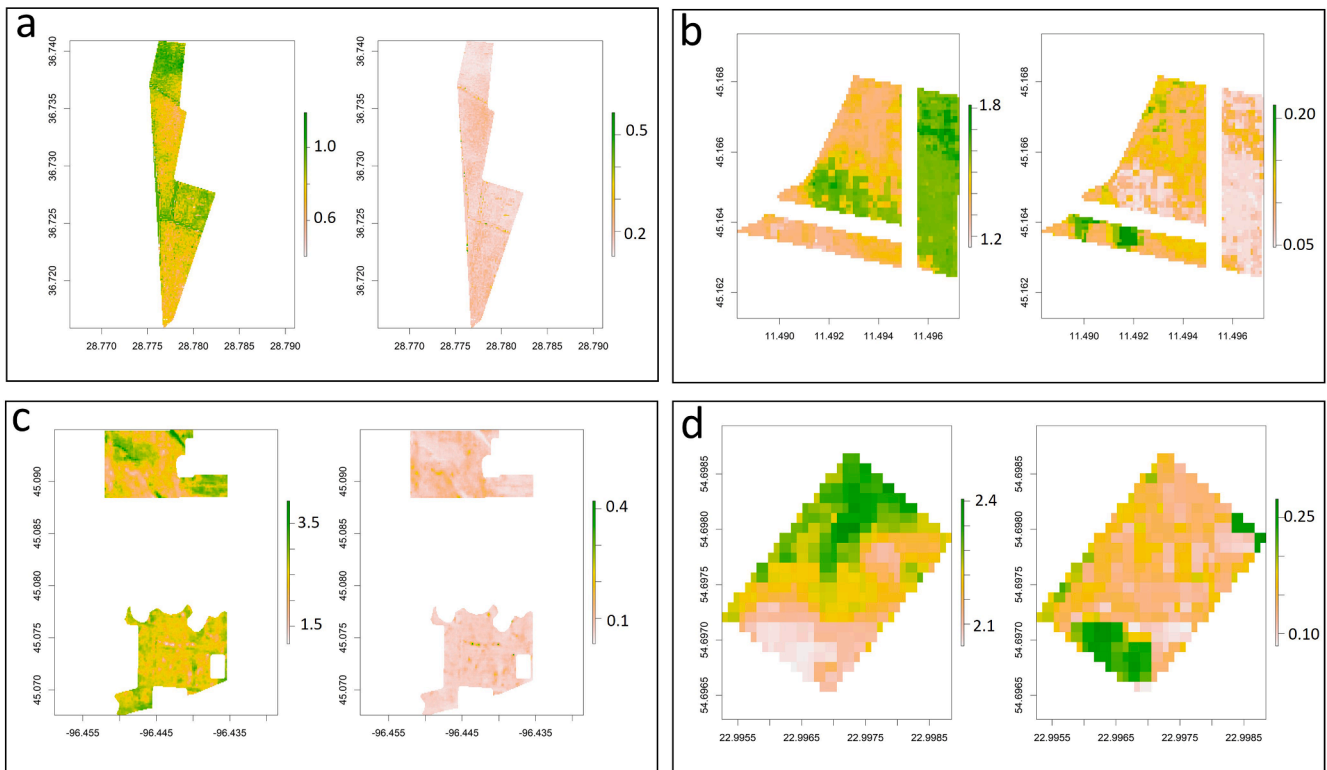

Fig. 11. SOC and uncertainty maps obtained using minS2WI + LMEM for the TUR_DAL site (a), Median + QRFxy for ITA_VAL site (b), Median + LMEM for USA_MIN site (c), R90 + QRF for LIT_RUM site (d).
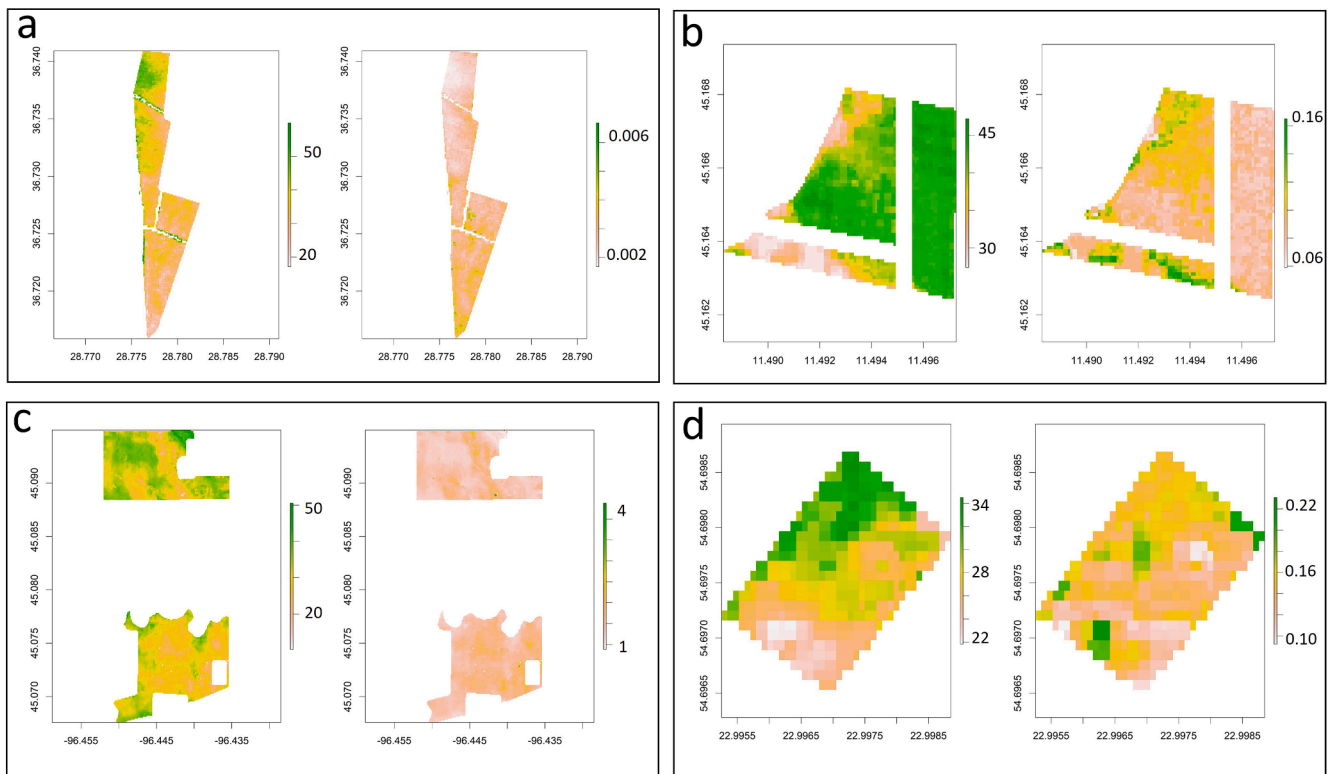
Fig. 12. Clay and uncertainty maps obtained using R90 + LMEM for the TUR_DAL site (a), Median + QRFxy for ITA_VAL site (b), R90 + LMEM for USA_MIN site (c), R90 + QRFxy for LIT_RUM site (d).

selection and can help to overcome the reduced availability of bare soil conditions. Our approaches to get SBSIs were adopted for a limited two-years satellite collection, nevertheless the temporal mosaicking increases the chance to find bare soil, under the assumption of the stability or very slow changes in SOC content or other soil properties if no drastic changes occur in terms of land use or soil management or as a result of extreme erosion processes (Castaldi, 2021). In this regard, the test sites were not affected by drastic changes or extreme erosion processes during the satellite collection period.

The four pixel-based temporal mosaicking approaches followed different strategies: increase the probability of detecting pure bare soil (maxBSI), selecting driest conditions (minS2WI and R90) and obtaining a median bare soil condition over the time series (Median). However, the algorithms search every acquisition date throughout the year, whereas the bare soil conditions are mainly concentrated in two periods: in Spring, after the seeding of summer crops, or at end of the Summer-beginning of the Autumn, after seeding winter crops, i.e. the periods between crop harvesting and the emergence of the following crop. The best period for the Italian sites and for most of the temporal mosaicking approaches is before the emergence of winter crop, thus in Summer, when the driest soil conditions usually occur in the Mediterranean region. However, the different strategies tested here involved the selection of different acquisition dates, although this variability also depends on the study sites. The R90 approach always involves the selection of images acquired in Autumn except for LIT_RUM field. Since this approach is based on the search for dry conditions, we can observe in Table 4 how the more frequent months fall in the middle of the Autumn for Mediterranean regions and for USA sites, while falling in June and September for two Lithuanian sites. This is due to higher amount of late summer – early autumn precipitation in Lithuania as compared to Italy and Türkiye. Most Median SBSI pixels were obtained from March to June except for the two Turkish sites where the driest condition delayed the selected dates to the end of the summer. For the Turkish sites, the period before winter crops is still the more frequent for maxBSI, minS2WI and

Median, however here the best period (August – October) is postponed as compared to Italian sites. This is because for both Turkish sites, maize is generally sown in June and harvested by the end of August.

For both USA sites, the best conditions can be found between April and May because from December to April, soil might be covered with snow. Therefore, in May there is a greater chance to find bare soil conditions just before maize germination. According to the results of the present study, only R90 seems quite stable across different climate conditions concerning the selection of the best satellite acquisition time. While the other composite approaches used more or less the same acquisition date for the same site, dates showed evident differences between test sites, mainly due to crop management and climate conditions.

4.3. Accounting for the bare soil condition

The dependence on site characteristics must first be emphasized, as through this various dataset, prediction performances vary according to agropedological characteristics as well as soil and crop management. As previously observed for satellite-based models at several scales (Vaudour et al., 2022), the sites displaying larger ranges of SOC contents, and in a lesser degree, clay contents, are prone to the highest performances regardless of SBSIs and models. Sampling density does not seem to be influent among the ten sites.

Depending on the SBSI temporal mosaicking approach, not only the performance of the spectral model varies but also the quality of the mapped output. For the most frequent months used to retrieve the synthetic bare soil images, the maxBSI and minS2WI displayed a within-field heterogeneity, involving a spotted look for the bare soil mosaics (Fig. 6). The elaboration of the temporal mosaic relies on correct sky conditions from one side, and on soil surface conditions from the other side. The searching for the maximum BSI, the minimum S2WI values or the maximum reflectance values along the satellite time may lead to select some specific pixels affected by non-detected environmental

disturbances (e.g. clouds or cloud shadows; Fig. 5), or possible instrumental issues or processing errors during the atmospheric correction applied to Top-Of-Atmosphere (TOA) (Zhou et al., 2022), hence spotted pattern. Regardless of the sky conditions, the temporal mosaicking, especially through the per-pixel approach, could put together pixels of several dates having different surface moisture conditions due to either rainfall events or ploughing or the presence of vegetation residues.

The Median and R90 approaches were conceived to get rid of such extreme values and therefore mitigate such issues, either originating from the atmospheric correction model itself, or from the cloud mask that is applied. At regional scale, Gomez et al. (2022) compared three atmospheric correction (AC) methods on Sentinel-2 images (MAJA, Sen2Cor, and Landsat Surface Reflectance Code) for clay content prediction, and pointed out that the acquisition date is more important than the AC method in terms of prediction accuracy for clay content. Nevertheless, they also observed that bare soil coverage selected using both NDVI and NBR2 thresholding varied depending on both acquisition dates and AC methods and that the Sen2Cor method, which is the one that we used here, provided the highest range of bare soil coverage along the acquisition dates. Further investigations deserve to be conducted to assess the effect of atmospheric correction on the estimation of SOC and other soil properties using time series. The spotted appearance obtained from maxBSI and minS2WI is not only an aesthetic issue, but it can lead to erroneous prediction models or misleading soil property maps, since the spots are pixels probably selected in different conditions as compared to the rest of the pixels within the fields. Moreover, the SOC and clay maps derived from spotted SBSIs have the highest uncertainty, while Median and R90 SBSIs demonstrated to outperform maxBSI and minS2WI both in terms of estimation accuracy and uncertainty (Table 5).

Vaudour et al. (2021) tested both per-pixel- and per-date-based mosaicking methods using Sentinel-2 collection at a regional scale in France. The best cross-validation results concerning SOC estimation by per-pixel-based approach were obtained using the combination of S2WI and NBR2 (RPIQ = 1.94), therefore confirming the capability of these two indices to provide useful bare soil mosaics not affected by extreme moisture contents and dry vegetation disturbance. However, the area covered by the mosaic was quite limited due to the strict thresholds of the two indices; therefore, the authors suggested the use of per-date approaches, which provided the same prediction accuracy while almost doubling the area covered by the bare soil mosaic. The poor prediction accuracy obtained in our work using maxBSI is in accordance with the results gained by Vaudour et al. (2021), which showed really low RPIQ cross-validation values using the BSI index (RPIQ = 1.60). However, although maxBSI often provided the lowest results among our test sites, and presumably owing to local scale and/or soil type, this approach generally showed better statistics, with RPIQ values ≥ 2.59 and up to 4.5, than those showed in Vaudour et al. (2021). Similarly, presumably owing to local scale and/or soil type, in our study, the use of S2WI (minS2WI) provided very different validation results depending on test site, ranging from an RPIQ of 1.28 in the Italian sites to 6.07 for USA_SDA, with very good results also for TUR_DAL (RPIQ = 2.72) and LIT_VAL (RPIQ = 1.90).

The Median SBSI has been successfully tested for SOC estimation over larger areas, by Luo et al. (2022) at regional scale using a six-years Landsat-8 time series and by Castaldi (2021) at continental scale using a three-years Sentinel-2 collection along with 144 LUCAS samples collected across Europe. Through the per-pixel approach, Castaldi (2021) obtained satisfactory results for SOC estimation. In the present work, the Median SBSI approach most of the times outperformed minS2WI and maxBSI approaches for SOC prediction. The better capability of the Median approach as compared to the others can be explained by the relative importance of visible bands for the estimation of the SOC content, as already shown by the VI analysis in Castaldi (2021), showing the high importance of the three Sentinel-2 visible bands (B2, B3 and B4). Organic matter has a relationship with electromagnetic radiation in

the visible region around 450, 590, and 664 nm (Ben-Dor et al., 1997), which corresponds to the Sentinel-2 bands, moreover the average soil conditions obtained by the Median SBSI bare soils may be less dry than those obtained by R90, as moisture content can enhance the difference in terms of organic matter content in the visible range (Castaldi et al., 2016). It should be noted that both BSI and S2WI do not, or only partially, use the visible bands, thus giving more relevance to the NIR and SWIR bands at the initial stage of bare pixel selection. Accuracy values related by R90 approach are higher than 90% in more than 50% of the cases for all the SOC estimation models, and for 60% of the cases only using QRFxy models (Table 6). Even though Median and minS2WI also provided some high Accuracy values, R90 outperformed the other SBSI approaches both for SOC and clay estimation. However the Accuracy for clay is higher than 90% only for 30% of the QRFxy models and for 40% of the LMM models using R90. According the Accuracy level required for EO-based applications reported by Andries et al. (2021) (>90%), R90 is the most promising SBSI for SOC monitoring, despite it mostly exploited satellite images acquired in late summer or autumn (Table 4) for the ten test sites; the solar altitude angles in this period are lower than in spring and early summer, thus making more difficult the atmospheric correction process (Vermote et al. 2016; Dvorakova et al., 2023). Moreover not considering the bidirectional reflectance distribution function (BRDF) effects could negatively affect Sentinel-2 applications, especially for images acquired far from spring time, thus for data not close to the orthogonal plane. This BRDF effects could be really significant in winter and showing increasing magnitude with wavelength, therefore with high negatively effects on SWIR (Roy et al., 2016). However, observing the VI bar plots for clay estimation using R90 (Fig. 8), it is obvious how B12 is really important and the difference between its VI value and the VI of the visible bands is quite clear, while such difference looks less noticeable for SOC prediction models by the Median SBSI approach. Although B12 is a quite broad band, it contains the spectral region affected by clay minerals and it is sensitive to water content, this can explain how the R90 approach is more efficient for estimating clay. Also, Gomez et al. (2022) observed how by selecting acquisition dates shortly after a rainfall event, the clay estimation accuracy drastically decreases, confirming the importance of selecting as dry soil conditions as possible to better highlight the contrast between different soil textures within the field; this because the differences in soil moisture due to soil texture are generally less detectable in very wet soil conditions, while the capacity for clay soils to hold water is more visible under dryer conditions. Moreover, R90 mostly selected images acquired after the winter crops seedings (late Summer – early Autumn), thus when the surface was smoothed, reducing the roughness and consequently reducing the anisotropic behavior of the soil and the BRDF effects. It should be notated that all the ten sites in this study are situated in very flat areas, reducing the anisotropy of the spectral response. However, considering the importance of the two SWIR bands both for SOC and clay estimation, the implementation of an approach to adjust Sentinel-2 reflectance data taking into account the BRDF effects, could lead to a not negligible improvement of the prediction accuracy (Roy et al., 2016), especially for rugged terrain and hilly regions where the anisotropic effect could be very consistent (Wen et al., 2018).

Gasmi et al. (2021) obtained satisfactory results for clay prediction using SBSI created computing the mean spectral reflectance from bare soil pixels along a Landsat-8 time series (RPIQ = 3.21). The highest spatial resolution of the Sentinel-2 data (10–20 m) as compared to Landsat-8 (30 m) can improve the estimation accuracy both for SOC and clay, as clearly shown in Castaldi, 2021 and Mzid et al., 2022. The high spectral resolution (more than 200 bands and narrow bandwidths) of the new generation of hyperspectral satellite imagers such as PRISMA (PRecursore IperSpettrale della Missione Applicativa) (Cogliati et al., 2021; Pignatti et al., 2012) and the Environmental Mapping and Analysis Program EnMAP (Guanter et al., 2015) can be successfully exploited for the estimation of soil properties, improving the accuracy as compared to multispectral sensors such as those on board of Sentinel-2

and Landsat-8 satellites (Castaldi et al., 2016; Mzid et al., 2022; Žížala et al., 2019; Wocher et al., 2022). The narrow bands, especially in the SWIR region, allow to properly exploit the spectral features related to organic matter and clay minerals. Nevertheless, the revisit time of EnMAP and PRISMA (27 – 29 days at nadir) is higher than those of the Sentinel-2 (5 days) and Landsat-8 (16 days), this can reduce the probability of finding cloud free images with soil in bare condition. Furthermore, the hyperspectral data assume a higher level of complexity for the processing chain as compared to multispectral data: this factor can be an issue for the implementation of automated mosaicking approaches such as those tested in this work. Mzid et al. (2021) estimated the frequency of bare soil – cloud-free images available over four cropland areas in Italy according to different revisit times, and they observed how the possibility of finding useful images becomes close to zero for a revisit time exceeding 15 days, especially in Northern Italy test area where a higher cloud frequency occurs. The planned Sentinel-10/CHIME (Copernicus Hyperspectral Imaging Mission for the Environment) (Nieke and Rast, 2019), will deliver a large amount of hyperspectral data every 10 – 12.5 days, thus facilitating the implementation of multi-temporal analysis for soil properties mapping. Moreover, the Sentinel-2 data can be exploited to figure out the best period for detecting bare soil conditions within a time series thanks to their high frequency of acquisition over the same area, and consequently optimizing the pre-processing and modelling efforts focusing on the best hyperspectral acquisition date and developing a multi-sensor and multi-temporal Earth Observation system.

4.4. Accounting for spatial structure and uncertainty analysis

All the work cited in the previous section did not use the geographical information related to soil samples to build hybrid prediction models. Nevertheless, Sentinel-2 spectral data retrieved from each pixel can be productively used as auxiliary variables in geostatistical or hybrid models because the relatively high spatial resolution is generally higher than the average distance between soil samples in the field (Vaudour et al., 2022). The hybrid methods, such as Regression Kriging, kriging with external drift, or LMEM combine regression models for the estimation of the coefficients of the covariates (deterministic part) and the spatial structure of the residual (stochastic part). The implementation of this kind of models using satellite data produced reliable soil properties prediction models (Mirzaee et al., 2016; Simbahan et al., 2006). The comparison between QRF and the other models (QRFxy and LMEM) highlighted the advantage of including the spatial autocorrelation both for clay and SOC estimation. In particular QRFxy models provided Accuracy values higher than 90% in 52.5% of the cases for SOC and 22.5% for clay, while the frequencies for QRF are 37.5% for SOC and 15% for clay (Table).

If the soil dataset was collected in the same field, there is a strong possibility that most measured soil properties would exhibit a spatial autocorrelation, therefore using a multivariate regression model without accounting for the spatial structure violates the sample independence assumption of the regression. Obviously, if a spatial structure exists, the implementation of spatial or hybrid models can lead to an improvement of the estimation accuracy. The results of the VI analysis shown in Figs. 8 and 9 clearly indicates the importance of the X and Y for the QRFxy models, and often their VI values are higher than those observed for the Sentinel-2 bands. The LMEMs showed the best performances in some test sites both for clay and SOC estimation, however, the differences in terms of RPIQ are not so evident as compared to QRFxy and moreover, LMEM often showed really high uncertainty of the estimated values (Table 6; Fig. 9b). A spatial structure of the QRF residual was detected both for SOC and clay in the TUR_KOC dataset according to the Moran's I test and, actually, the LMEM models improved the estimation accuracy as compared to QRF and QRFxy. Yet, the standard deviation of the estimates is really high in this site. TUR_KOC site is not a single field, but it is a set of adjacent fields, some of which in the

northern side, irrigated by a center-pivot system, and this can explain such high uncertainty. Consequently, the tested spatial approaches (QRFxy and LMEM) seem to be most effective to determine the SOC and clay variation in singular field, while over larger regions the differences in agronomic and soil management might hide or change natural spatial variability of soil properties, making more difficult the implementation of spatial models (Castaldi et al., 2019c).

Also, ITA_VAL site is composed of three fields and in this case, due to a management difference between the fields, there is not a spatial structure in the soil data and the uncertainty of the models is very high. On the contrary, other single-field test sites, such as TUR_DAL or LIT_RUM for Median and R90 models, showed uncertainty levels similar to the QRFxy models. LMEM is a hybrid method that includes geostatistics and therefore the estimates provided by kriging interpolation are smooth and the kriging variance, from which we retrieved the "pointwise uncertainty", as defined here, provides quantitative information about the smoothness (Deutsch, 2003). Therefore, even though the prediction error is low, the higher the variance, the higher the smoothness and the uncertainty of the SOC and clay estimates. It should be specified that the uncertainty that is computed here, is not exactly the one defined from confidence intervals. A further development of our study would consist of comparing approaches of uncertainty assessment, for instance the pointwise uncertainty previously defined by Zaouche et al. (2017) and that retrieved by Vaysse and Lagacherie (2017). In general, the combination of R90 or Median SBSI and spatial models (QRFxy or LMEM) outperformed the other tested approaches. The SOC predicted values obtained by the R90_QRFxy models showed in Fig. 13a are very close to the 1:1 line for all the ten test sites, thus for the whole SOC range, while in Fig. 13b, the predicted values obtained by maxB-SI_QRF are scattered and mostly grouped around the average SOC value for each national group. For clay estimation also, the predicted values gained by the R90_LMEM models showed in Fig. 13c are less dispersed compared to those obtained using maxBSI_QRF models (Fig. 13d), especially for the Turkish and Italian samples that have the highest clay content.

The high sampling density in most of the ten sites raises the question of whether the use of satellites bands as covariates provides an advantage over geostatistical approaches for the estimation of soil properties. It should be noted that the minimum number of sampling units to estimate an accurate variogram function for geostatistical prediction is 100 (Kerry and Oliver, 2007), while the use of the REML, the same approach used here for LMEMs, allows the estimation of the variogram with fewer sampling units (Kerry and Oliver, 2007). Except for TUR_KOC, less than 100 were collected within the test sites, therefore the use of satellite-retrieved information allowed mapping SOC and clay content using fewer samples than necessary for the implementation of geostatistical approaches. However, if on one hand the sampling density for most of the ten sites is still considerably high, on the other hand, observing the prediction accuracies of the test sites, the density does not seem to influence the performances. Therefore, a compromise needs to be found between estimation accuracy and sampling density and consequently the sampling cost. According to Castaldi et al. (2019b), the ratio between accuracy and sampling density can be optimized by chosing algorithms based on the feature space, instead of the geographical space, where the covariate data are the Sentinel-2 bands. Future investigations should focus on strategies and algorithms for the reduction and the optimization of the sampling density for the calibration of SOC and clay prediction models at local scale.

5. Conclusions

Focused on the feasibility of Sentinel-2 based approaches for the detailed mapping of topsoil clay and SOC contents at the local scale, this study built several two-years-Sentinel-2 temporal mosaics or SBSI, for cropland sites of contrasted climate and soil types across the Northern hemisphere. Relying on a number of spectral indices and a pixelwise
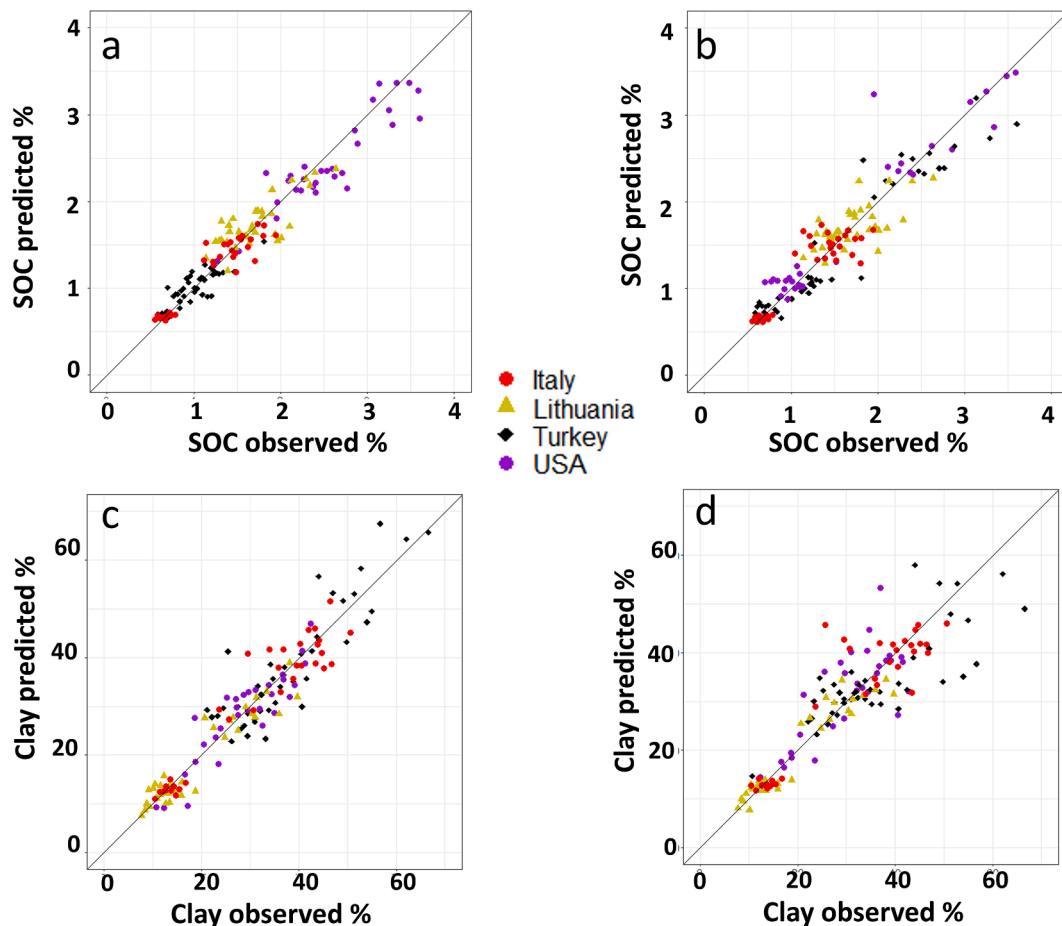
Fig. 13. scatterplots of the validation results using the combination of a) R90 + QRFxy models, b) maxBSI + QRF, c) R90 + LMEM, d) maxBSI + QRF.

basis, it focused on *i)* pure bare soil condition, *ii)* driest soil condition, *iii)* average bare soil condition and *iv)* dry soil conditions excluding extreme reflectance values. Overall performances were reasonably accurate: the average RPIQ of the best performances among the test sites was 2.50 both for SOC and clay. However, both accuracy level and uncertainties were mainly influenced by site characteristics of soil and soil management, in combination with the SBSI approach and the model type.

The models including a spatial component were the best performing, especially QRFxy models (average RPIQ = 2.13), as compared to models only using Sentinel-2 bands as independent variables (average RPIQ = 1.80), while the best spatial mosaicking approaches mostly were *iii)* or *iv)*. The most frequent best combination of SBSI and model type was Median and QRFxy for SOC, while for clay estimation, it was less obvious and in favor of R90 and LMEM. According to the validation results showed in this work, R90 is the most promising SBSI approach for SOC and clay estimation and it could be successfully used for SOC monitoring: R90 approach outperformed the other SBSI approaches providing Accuracy values higher than 90% in 53.3% of validation tests for SOC and in 26.7% for clay.

The assessment of pointwise uncertainty as we defined it appears to be key as some accurate estimations may actually be very uncertain. Future challenges will consist of looking further into the possible reasons why models vary according to site, as well as the possible reasons for such uncertainty, presumably linked to the assemblage of several pixels taken at several dates with heterogeneous soil surface preparation, soil surface moisture and roughness.

Declaration of Competing Interest

The authors declare that they have no known competing financial interests or personal relationships that could have appeared to influence the work reported in this paper.

References

Andries, A., Morse, S., Murphy, R.J., Lynch, J., Mota, B., Woolliams, E.R., 2021. Can Current Earth Observation Technologies Provide Useful Information on Soil Organic Carbon Stocks for Environmental Land Management Policy? Sustainability 13, 12074. https://doi.org/10.3390/SU132112074.

Arrouays, D., Grundy, M.G., Hartemink, A.E., Hempel, J.W., Heuvelink, G.B.M., Hong, S. Y., Lagacherie, P., Lelyk, G., McBratney, A.B., McKenzie, N.J., Mendonca-Santos, M. D.L., Minasny, B., Montanarella, L., Odeh, I.O.A., Sanchez, P.A., Thompson, J.A., Zhang, G.L., 2014. GlobalSoilMap: Toward a Fine-Resolution Global Grid of Soil Properties. Advances in Agronomy 125, 93–134. https://doi.org/10.1016/B978-0-12-800137-0.00003-0.

Ben-Dor, E., 2002. Quantitative remote sensing of soil properties. In: Advances in Agronomy. Academic Press, pp. 173–243.

Ben-Dor, E., Inbar, Y., Chen, Y., 1997. The reflectance spectra of organic matter in the visible near-infrared and short wave infrared region (400–2500 nm) during a controlled decomposition process. Remote Sens. Environ. 61, 1–15. https://doi.org/10.1016/S0034-4257(96)00120-4.

Bouyoucos, G.J., 1951. A Recalibration of the Hydrometer Method for Making Mechanical Analysis of Soils1. Agron J. 43, 434–438. https://doi.org/10.2134/AGRONJ1951.00021962004300090005X.

Brockett, B.F.T., Browne, A.L., Beanland, A., Whitfield, M.G., Watson, N., Blackburn, G.A., Bardgett, R.D., 2019. Guiding carbon farming using interdisciplinary mixed methods mapping. People Nat. 1, 191–203. https://doi.org/10.1002/PAN3.24/SUPPINFO.

Bukantis, A., 2009. Agroclimatic zoning. Lithuanian National Atlas. National Land Service under the Ministry of Agriculture, Vilnius.

Cao, Y., Bao, N., Liu, S., Zhao, W., Li, S., 2020. Reducing moisture effects on soil organic carbon content prediction in visible and near-infrared spectra with an external parameter othogonalization algorithm (MA Naeth, Ed.). Can. J. Soil Sci. 100, 253–262.

Castaldi, F., 2021. Sentinel-2 and landsat-8 multi-temporal series to estimate topsoil properties on croplands. Remote Sens. (Basel) 13. https://doi.org/10.3390/rs13173345.

Castaldi, F., Chabrillat, S., Don, A., van Wesemael, B., 2019a. Soil organic carbon mapping using LUCAS topsoil database and Sentinel-2 data: An approach to reduce soil moisture and crop residue effects. Remote Sens. (Basel) 11. https://doi.org/10.3390/rs11182121.

Castaldi, F., Chabrillat, S., van Wesemael, B., 2019b. Sampling strategies for soil property mapping using multispectral Sentinel-2 and hyperspectral EnMAP satellite data. Remote Sens. (Basel) 11. https://doi.org/10.3390/rs11030309.

Castaldi, F., Hueni, A., Chabrillat, S., Ward, K., Buttafuoco, G., Bomans, B., Vreys, K., Brell, M., van Wesemael, B., 2019c. Evaluating the capability of the Sentinel 2 data for soil organic carbon prediction in croplands. ISPRS J. Photogramm. Remote Sens. 147 https://doi.org/10.1016/j.isprsjprs.2018.11.026.

Castaldi, F., Palombo, A., Santini, F., Pascucci, S., Pignatti, S., Casa, R., 2016. Evaluation of the potential of the current and forthcoming multispectral and hyperspectral imagers to estimate soil texture and organic carbon. Remote Sens. Environ. 179 https://doi.org/10.1016/j.rse.2016.03.025.

Chabrillat, S., Ben-Dor, E., Cierniewski, J., Gomez, C., Schmid, T., van Wesemael, B., 2019. Imaging Spectroscopy for Soil Mapping and Monitoring. Surv Geophys 40, 361–399. https://doi.org/10.1007/S10712-019-09524-0/TABLES/2.

Chen, L., Smith, P., Yang, Y., 2015. How has soil carbon stock changed over recent decades? Glob. Chang. Biol. 21, 3197–3199. https://doi.org/10.1111/GCB.12992.

Cogliati, S., Sarti, F., Chiarantini, L., Cosi, M., Lorusso, R., Lopinto, E., Miglietta, F., Genesio, L., Guanter, L., Damm, A., Pérez-López, S., Scheffler, D., Tagliabue, G., Panigada, C., Rascher, U., Dowling, T.P.F., Giardino, C., Colombo, R., 2021. The PRISMA imaging spectroscopy mission: overview and first performance analysis. Remote Sens. Environ. 262, 112499 https://doi.org/10.1016/J.RSE.2021.112499.

Demattê, J.A.M., Fongaro, C.T., Rizzo, R., Safanelli, J.L., 2018. Geospatial Soil Sensing System (GEOS3): A powerful data mining procedure to retrieve soil spectral reflectance from satellite images. Remote Sens. Environ. 212, 161–175. https://doi.org/10.1016/J.RSE.2018.04.047.

Deutsch, C.V., 2003. Geostatistics. Encyclopedia Phys. Sci. Technol. 697–707 https://doi.org/10.1016/B0-12-227410-5/00869-3.

Diek, S., Fornallaz, F., Schaepman, M.E., de Jong, R., 2017. Barest Pixel Composite for Agricultural Areas Using Landsat Time Series. Remote Sens. 9, 1245. https://doi.org/10.3390/RS9121245.

Dvorakova, K., Heiden, U., Pepers, K., Staats, G., van Os, G., van Wesemael, B., 2023. Improving soil organic carbon predictions from a Sentinel–2 soil composite by assessing surface conditions and uncertainties. Geoderma 429, 116128. https://doi.org/10.1016/J.GEODERMA.2022.116128.

Dvorakova, K., Heiden, U., van Wesemael, B., 2021. Sentinel-2 Exposed Soil Composite for Soil Organic Carbon Prediction. Remote Sens. 13, 1791. https://doi.org/10.3390/RS13091791.

El Hajj, M., Baghdadi, N., Zribi, M., Bazzi, H., 2017. Synergic use of Sentinel-1 and Sentinel-2 image for operational soil moisture mapping at high spatial resolution over agricultural areas. Remote Sens. (Basel) 9, 1292. https://doi.org/10.3390/rs9121292.

European Commission, Directorate-General for Agriculture and Rural Development, 2021. Evaluation support study on the impact of the CAP on sustainable management of the soil : final report, Publications Office. https://data.europa.eu/doi/10.2762/799605.

Fontana, A., Mozzi, P., Marchetti, M., 2014. Alluvial fans and megafans along the southern side of the Alps. Sediment Geol. 301, 150–171. https://doi.org/10.1016/J.SEDGEO.2013.09.003.

Garlato, A., Obber, S., Vinci, I., Minelli, R., Pocaterra, F., Sartori, G., Giandon, P., 2005. Carta dei suoli della Regione Veneto alla scala 1:250.000. ARPAV, Treviso, 1 map, 3 vol, 383 pp ISBN 88-7504-097-4.

Gasmi, A., Gomez, C., Lagacherie, P., Zouari, H., Laamrani, A., Chehbouni, A., 2021. Mean spectral reflectance from bare soil pixels along a Landsat-TM time series to increase both the prediction accuracy of soil clay content and mapping coverage. Geoderma 388, 114864. https://doi.org/10.1016/J.GEODERMA.2020.114864.

Gholizadeh, A., Žižala, D., Saberioon, M., Borůvka, L., 2018. Soil organic carbon and texture retrieving and mapping using proximal, airborne and Sentinel-2 spectral imaging. Remote Sens. Environ. 218, 89–103. https://doi.org/10.1016/J.RSE.2018.09.015.

Gomez, C., Vaudour, E., Féret, J.B., de Boissieu, F., Dharumarajan, S., 2022. Topsoil clay content mapping in croplands from Sentinel-2 data: Influence of atmospheric correction methods across a season time series. Geoderma 423, 115959. https://doi.org/10.1016/J.GEODERMA.2022.115959.

Guanter, L., Kaufmann, H., Segl, K., Foerster, S., Rogass, C., Chabrillat, S., Kuester, T., Hollstein, A., Rossner, G., Chlebek, C., Straif, C., Fischer, S., Schrader, S., Storch, T., Heiden, U., Mueller, A., Bachmann, M., Mühle, H., Müller, R., Habermeyer, M., Ohndorf, A., Hill, J., Buddenbaum, H., Hostert, P., van der Linden, S., Leitão, P.J., Rabe, A., Doerffer, R., Krasemann, H., Xi, H., Mauser, W., Hank, T., Locherer, M., Rast, M., Staenz, K., Sang, B., 2015. The EnMAP Spaceborne Imaging Spectroscopy Mission for Earth Observation. Remote Sensing 7, 8830–8857. https://doi.org/10.3390/RS70708830.

IUSS Working Group WRB. 2015. World Reference Base for Soil Resources 2014, update 2015 Internatio-nal soil classification system for naming soils and creating legends for soil maps. World Soil Re-sources Reports No. 106. FAO, Rome.

Kerry, R., Oliver, M.A., 2007. Comparing sampling needs for variograms of soil properties computed by the method of moments and residual maximum likelihood. Geoderma 140 (4), 383–396. https://doi.org/10.1016/J.GEODERMA.2007.04.019.

Knadel, M., Castaldi, F., Barbetti, R., Ben-Dor, E., Gholizadeh, A., & Lorenzetti, R. (2022). Mathematical techniques to remove moisture effects from visible–near-infrared–shortwave-infrared soil spectra—review. https://doi.org/10.1080/05704928.2022.2128365.

Kuhn, M., 2008. Building Predictive Models in R Using the caret Package. J Stat Softw 28, 1–26. https://doi.org/10.18637/JSS.V028.I05.

Li, Z., Shen, H., Weng, Q., Zhang, Y., Dou, P., Zhang, L., 2022. Cloud and cloud shadow detection for optical satellite imagery: Features, algorithms, validation, and prospects. ISPRS J. Photogramm. Remote Sens. 188, 89–108. https://doi.org/10.1016/J.ISPRSJPRS.2022.03.020.

Liaw, A., Wiener, M., 2002. Classification and Regression by randomForest 2.

Loiseau, T., Chen, S., Mulder, V.L., Román Dobarco, M., Richer-de-Forges, A.C., Lehmann, S., Bourennane, H., Saby, N.P.A., Martin, M.P., Vaudour, E., Gomez, C., Lagacherie, P., Arrouays, D., 2019. Satellite data integration for soil clay content modelling at a national scale. Int. J. Appl. Earth Obs. Geoinf. 82, 101905 https://doi.org/10.1016/j.jag.2019.101905.

Luo, C., Zhang, X., Meng, X., Zhu, H., Ni, C., Chen, M., Liu, H., 2022. Regional mapping of soil organic matter content using multitemporal synthetic Landsat 8 images in Google Earth Engine. Catena (Amst) 209. https://doi.org/10.1016/J.CATENA.2021.105842.

Main-Knorn, M., Pflug, B., Louis, J., Debaecker, V., Müller-Wilm, U., Gascon, F., 2017. Sen2Cor for Sentinel-2 3. https://doi.org/10.1117/12.2278218.

Meinshausen, N., 2006. Quantile Regression Forests. J. Mach. Learn. Res. 7, 983–999.

Meinshausen, N., Maintainer, L.S., 2015. Package "quantregForest." Minasny, B., McBratney, A.B., Bellon-Maurel, V., Roger, J.-M., Gobrecht, A., Ferrand, L. & Joalland, S. 2011. Removing the effect of soil moisture from NIR diffuse reflectance spectra for the prediction of soil organic carbon. Geoderma, 167–168, 118–124.

Minasny, B., Malone, B.P., McBratney, A.B., Angers, D.A., Arrouays, D., Chambers, A., Chaplot, V., Chen, Z.S., Cheng, K., Das, B.S., Field, D.J., Gimona, A., Hedley, C.B., Hong, S.Y., Mandal, B., Marchant, B.P., Martin, M., McConkey, B.G., Mulder, V.L., O'Rourke, S., Richer-de-Forges, A.C., Odeh, I., Padarian, J., Paustian, K., Pan, G., Poggio, L., Savin, I., Stolbovoy, V., Stockmann, U., Sulaeman, Y., Tsui, C.C., Vågen, T.G., van Wesemael, B., Winowiecki, L., 2017. Soil carbon 4 per mille. Geoderma 292, 59–86. https://doi.org/10.1016/J.GEODERMA.2017.01.002.

Mirzaee, S., Ghorbani-Dashtaki, S., Mohammadi, J., Asadi, H., Asadzadeh, F., 2016. Spatial variability of soil organic matter using remote sensing data. Catena (Amst) 145, 118–127. https://doi.org/10.1016/J.CATENA.2016.05.023.

Mirzaei, S., Darvishi Boloorani, A., Bahrami, H.A., Alavipanah, S.K., Mousivand, A., Mouazen, A.M., 2022. Minimising the effect of moisture on soil property prediction accuracy using external parameter orthogonalization. Soil Tillage Res. 215, 105225.

Mzid, N., Castaldi, F., Tolomio, M., Pascucci, S., Casa, R., Pignatti, S., 2022. Evaluation of Agricultural Bare Soil Properties Retrieval from Landsat 8, Sentinel-2 and PRISMA Satellite Data. Remote Sens (Basel) 14. https://doi.org/10.3390/rs14030714.

Mzid, N., Pignatti, S., Huang, W., Casa, R., 2021. An Analysis of Bare Soil Occurrence in Arable Croplands for Remote Sensing Topsoil Applications. Remote Sensing 13, 474. https://doi.org/10.3390/RS13030474.

Nieke, J., Rast, M., 2019. Status: Copernicus Hyperspectral Imaging Mission for the Environment (CHIME). Int. Geosci. Remote Sensing Symposium (IGARSS) 4609–4611. https://doi.org/10.1109/IGARSS.2019.8899807.

Odeh, I.O.A., McBratney, A.B., Chittleborough, D.J., 1995. Further results on prediction of soil properties from terrain attributes: heterotopic cokriging and regression-kriging. Geoderma 67, 215–226. https://doi.org/10.1016/0016-7061(95)00007-B.

Panagos, P., Borrelli, P., Meusburger, K., Alewell, C., Lugato, E., Montanarella, L., 2015. Estimating the soil erosion cover-management factor at the European scale. Land Use Policy 48, 38–50. https://doi.org/10.1016/J.LANDUSEPOL.2015.05.021.

Paszkuta, M., Zapadka, T., Krężel, A., 2019. Assessment of cloudiness for use in environmental marine research. https://doi.org/10.1080/01431161.2019.163369740, 9439-9459. 10(1080/01431161), pp. 1633697, 2019.

Peel, M.C., Finlayson, B.L., McMahon, T.A., 2007. Updated world map of the Köppen-Geiger climate classification. Hydrol Earth Syst Sci 11, 1633–1644. https://doi.org/10.5194/HESS-11-1633-2007.

Pignatti, S., Acito, N., Amato, U., Casa, R., de Bonis, R., Diani, M., Laneve, G., Matteoli, S., Palombo, A., Pascucci, S., Romano, F., Santini, F., Simoniello, T., Ananasso, C., Zoffoli, S., Corsini, G., Cuomo, V., 2012. Development of algorithms and products for supporting the Italian hyperspectral PRISMA mission: The SAP4PRISMA project. International Geoscience and Remote Sensing Symposium (IGARSS) 127–130. https://doi.org/10.1109/IGARSS.2012.6351620.

Piikki, K., Wetterlind, J., Söderström, M., Stenberg, B., 2021. Perspectives on validation in digital soil mapping of continuous attributes—A review. Soil Use Manag 37, 7–21. https://doi.org/10.1111/SUM.12694.

Pribyl, D.W., 2010. A critical review of the conventional SOC to SOM conversion factor. Geoderma 156, 75–83. https://doi.org/10.1016/J.GEODERMA.2010.02.003.

Rienzi, E.A., Mijatovic, B., Mueller, T.G., Matocha, C.J., Sikora, F.J., Castrignanò, A., 2014. Prediction of soil organic carbon under varying moisture levels using reflectance spectroscopy. Soil Sci Soc Am J. 78, 958.

Rikimaru, A., Roy, P.S., Miyatake, S., 2002. Tropical forest cover density mapping. Trop Ecol 43, 39–47.

Roy, D.P., Zhang, H.K., Ju, J., Gomez-Dans, J.L., Lewis, P.E., Schaaf, C.B., Sun, Q., Li, J., Huang, H., Kovalskyy, V., 2016. A general method to normalize Landsat reflectance data to nadir BRDF adjusted reflectance. Remote Sens. Environ. 176, 255–271. https://doi.org/10.1016/J.RSE.2016.01.023.

R Core Team., 2022. R: A language and environment for statistical computing. R Foundation for Statistical Computing, Vienna, Austria. URL https://www.R-project.org/.

SDSU (2006). South Dakota State University. 2006. Soil testing procedures in use at the South Dakota State Soil Testing and Plant Analysis Laboratory. SDSU.

Shi, P., Six, J., Sila, A., Vanlauwe, B., van Oost, K., 2022. Towards spatially continuous mapping of soil organic carbon in croplands using multitemporal Sentinel-2 remote sensing. ISPRS J. Photogramm. Remote Sens. 193, 187–199. https://doi.org/10.1016/J.ISPRSJPRS.2022.09.013.

Simbahan, G.C., Dobermann, A., Goovaerts, P., Ping, J., Haddix, M.L., 2006. Fine-resolution mapping of soil organic carbon based on multivariate secondary data. Geoderma 132, 471–489. https://doi.org/10.1016/J.GEODERMA.2005.07.001.

Tziolas, N., Tsakiridis, N., Chabrillat, S., Demattê, J.A.M., Ben-Dor, E., Gholizadeh, A., Zalidis, G., van Wesemael, B., 2021. Earth Observation Data-Driven Cropland Soil Monitoring: A Review. Remote Sens. 13, 4439. https://doi.org/10.3390/RS13214439.

Stenberg, B., Viscarra Rossel, R.A., Mouazen, A.M., Wetterlind, J., 2010. Visible and Near Infrared Spectroscopy in Soil Science. In: Advances in Agronomy. Elsevier, pp. 163–215.

Urbina-Salazar, D., Vaudour, E., Baghdadi, N., Ceschia, E., Richer-De-forges, A.C., Lehmann, S., Arrouays, D., 2021. Using sentinel-2 images for soil organic carbon content mapping in croplands of southwestern france. The usefulness of sentinel-1/2 derived moisture maps and mismatches between sentinel images and sampling dates. Remote Sens. 13 https://doi.org/10.3390/rs13245115.

Vaudour, E., Gholizadeh, A., Castaldi, F., Saberioon, M., Borůvka, L., Urbina-Salazar, D., Fouad, Y., Arrouays, D., Richer-De-Forges, A.C., Biney, J., Wetterlind, J., van Wesemael, B., 2022. Satellite Imagery to Map Topsoil Organic Carbon Content over Cultivated Areas: An Overview. Remote Sens. 14, 2917. https://doi.org/10.3390/RS14122917.

Vaudour, E., Gomez, C., Lagacherie, P., Loiseau, T., Baghdadi, N., Urbina-Salazar, D., Loubet, B., Arrouays, D., 2021. Temporal mosaicking approaches of Sentinel-2 images for extending topsoil organic carbon content mapping in croplands. Int. J. Appl. Earth Obs. Geoinf. 96, 102277 https://doi.org/10.1016/J.JAG.2020.102277.

Vaudour, E., Gomez, C., Loiseau, T., Baghdadi, N., Loubet, B., Arrouays, D., Ali, L., Lagacherie, P., 2019. The Impact of Acquisition Date on the Prediction Performance of Topsoil Organic Carbon from Sentinel-2 for Croplands. Remote Sens. 11, 2143. https://doi.org/10.3390/RS11182143.

Vaysse, K., Lagacherie, P., 2017. Using quantile regression forest to estimate uncertainty of digital soil mapping products. Geoderma 291, 55–64. https://doi.org/10.1016/J.GEODERMA.2016.12.017.

Vermote, E., Justice, C., Claverie, M., Franch, B., 2016. Preliminary analysis of the performance of the Landsat 8/OLI land surface reflectance product. Remote Sens. Environ. 185, 46–56. https://doi.org/10.1016/J.RSE.2016.04.008.

Wen, J., Liu, Q., Xiao, Q., Liu, Q., You, D., Hao, D., Wu, S., Lin, X., 2018. Characterizing land surface anisotropic reflectance over rugged terrain: A review of concepts and recent developments. Remote Sens. 10 (3), 370. https://doi.org/10.3390/RS10030370.

Wocher, M., Berger, K., Verrelst, J., Hank, T., 2022. Retrieval of carbon content and biomass from hyperspectral imagery over cultivated areas. ISPRS J. Photogramm. Remote Sens. 193, 104–114. https://doi.org/10.1016/J.ISPRSJPRS.2022.09.003.

Zaouche, M., Bel, L., Vaudour, E., 2017. Geostatistical mapping of topsoil organic carbon and uncertainty assessment in Western Paris croplands (France). Geoderma Reg. 10, 126–137. https://doi.org/10.1016/J.GEODRS.2017.07.002.

Zhou, Q., Zhu, Z., Xian, G., Li, C., 2022. A novel regression method for harmonic analysis of time series. ISPRS J. Photogramm. Remote Sens. 185, 48–61. https://doi.org/10.1016/J.ISPRSJPRS.2022.01.006.

Žížala, D., Minařík, R., Zádorová, T., 2019. Soil Organic Carbon Mapping Using Multispectral Remote Sensing Data: Prediction Ability of Data with Different Spatial and Spectral Resolutions. Remote Sens. 11, 2947. https://doi.org/10.3390/RS11242947.